Protective and Nanoporous Alumina Films Studied in situ by X-ray and Electrochemical Methods

Evertsson, Jonas

2017

Document Version:
Publisher's PDF, also known as Version of record

Protective and Nanoporous Alumina Films Studied *in situ* by X-ray and Electrochemical Methods

Jonas Evertsson

LUND
UNIVERSITY

DOCTORAL THESIS
by due permission of the Faculty of Science, Lund University, Sweden.
To be defended in the Rydberg Lecture Hall at the Department of Physics,
26 January 2018 at 09:15.

Faculty opponent
Prof. Chris Lucas, University of Liverpool

Organization
LUND UNIVERSITY, Division of Synchrotron Radiation Research, Department of Physics

Box 118, S-221 00 Lund

Author: Jonas Evertsson

Document name:
DOCTORAL THESIS

Date of disputation: 26 January 2018

Sponsoring organization

Title and subtitle:

Protective and Nanoporous Alumina Films Studied *in situ* by X-ray and Electrochemical Methods

Abstract

In this thesis, the studies of native and anodic oxides on both aluminum model single crystal surfaces as well as on aluminum alloys found in applications are presented. The focus has been on the characterization *in situ* as the oxide is growing by an electrochemical process called anodization. For the investigations, a combination of various X-ray scattering and spectroscopy methods, as well as electrochemical methods were used. In addition, scanning electron microscopy and atomic force microscopy were used for ex situ characterization after the oxide growth.

From thickness measurements of native oxide films, it was found that the film was thicker on the aluminum alloys than on the pure aluminum single crystal surfaces. It was also found that the thicknesses obtained from the electrochemical impedance spectroscopy were thinner than from X-ray reflectivity and X-ray photoelectron spectroscopy.

The anodic oxide film was studied during anodization in sodium sulfate and citrate buffer solutions using a combination of X-ray reflectivity and electrochemical impedance spectroscopy. It was found with both techniques that the film thickness increased with anodization potential, but the thicknesses obtained from electrochemical impedance spectroscopy were thinner. The difference was attributed to a porous layer that is difficult to determine with impedance spectroscopy. It was also found that the electrochemical resistance of the oxide was less on the alloys than on the pure aluminum single crystals, which was partly attributed to the alloying elements. Finally, it was found that the anodic oxides formed in the buffer solution were less rough than the oxides formed in the sodium sulfate solutions. Generally, the approach provides the possibility of studying both the electrochemical and structural properties of anodic oxides, which in the future also can be used for corrosion studies of aluminum materials as well as other materials.

The growth of self-ordered nanoporous anodic aluminum oxides was studied using grazing-incidence transmission small-angle X-ray scattering by which the interpore distance between the pores, domain size of ordered pores and thickness of the oxide could be followed during the anodization process. In 0.3 M sulfuric acid at 25 V and 0.3 M oxalic acid at 40 V the interpore distance and domain length increased with time, where the final interpore distance and domain length were larger in the case of oxalic acid at 40 V. In both electrolytes it was found that the single crystal orientation did not significantly influence the interpore distance or the domain length. However, it was found that the orientation had a strong influence on the growth rate, especially during anodization in oxalic acid. The electrodeposition of tin into the pores of the oxides was also studied with X-ray fluorescence and grazing-incidence transmission small-angle X-ray scattering, and it was possible to follow the increase of tin in the pores during the deposition. Generally, the method and the approach provides a tool for high statistical and temporal investigations during the growth as well as during possible applications of the nanoporous oxides, which is not obtained with standard microscopy methods that are classically used for studies of these systems.

Key words:

XRR, XPS, XRF, GTSAXS, EIS, Synchrotron radiation, Native oxide, Anodization, Anodic aluminum oxide, Nanoporous aluminum oxide, Single crystal, Aluminum alloys, *In situ*

Classification system and/or index terms (if any)

Supplementary bibliographical information

Language
English

ISSN and key title

ISBN
978-91-7753-435-8 (print)
978-91-7753-436-5 (pdf)

Recipient's notes

Number of pages 214

Price

Security classification

Protective and Nanoporous Alumina Films Studied *in situ* by X-ray and Electrochemical Methods

Jonas Evertsson

Doctoral Thesis
2018

LUND
UNIVERSITY

Division of Synchrotron Radiation Research
Department of Physics
Lund University

Division of Synchrotron Radiation Research
Department of Physics
Lund University

ISBN:
978-91-7753-435-8 (print)
978-91-7753-436-5 (pdf)

Printed in Sweden by Media-Tryck, Lund University
Lund 2018

Abstract

In this thesis, the studies of native and anodic oxides on both aluminum model single crystal surfaces as well as on aluminum alloys found in applications are presented. The focus has been on the characterization *in situ* as the oxide is growing by an electrochemical process called anodization. For the investigations, a combination of various X-ray scattering and spectroscopy methods, as well as electrochemical methods were used. In addition, scanning electron microscopy and atomic force microscopy were used for *ex situ* characterization after the oxide growth.

From thickness measurements of native oxide films, it was found that the film was thicker on the aluminum alloys than on the pure aluminum single crystal surfaces. It was also found that the thicknesses obtained from the electrochemical impedance spectroscopy were thinner than from X-ray reflectivity and X-ray photoelectron spectroscopy.

The anodic oxide film was studied during anodization in sodium sulfate and citrate buffer solutions using a combination of X-ray reflectivity and electrochemical impedance spectroscopy. It was found with both techniques that the film thickness increased with anodization potential, but the thicknesses obtained from electrochemical impedance spectroscopy were thinner. The difference was attributed to a porous layer that is difficult to determine with impedance spectroscopy. It was also found that the electrochemical resistance of the oxide was less on the alloys than on the pure aluminum single crystals, which was partly attributed to the alloying elements. Finally, it was found that the anodic oxides formed in the buffer solution were less rough than the oxides formed in the sodium sulfate solutions. Generally, the approach provides the possibility of studying both the electrochemical and structural properties of anodic oxides, which in the future also can be used for corrosion studies of aluminum materials as well as other materials.

The growth of self-ordered nanoporous anodic aluminum oxides was studied using grazing-incidence transmission small-angle X-ray scattering by which the interpore distance between the pores, domain size of ordered pores and thickness of the oxide could be followed during the anodization process. In 0.3 M sulfuric acid at 25 V and 0.3 M oxalic acid at 40 V the interpore distance and domain length increased with time, where the final interpore distance and domain length were larger in the case of oxalic acid at 40 V. In both electrolytes it was found that the single crystal

orientation did not significantly influence the interpore distance or the domain length. However, it was found that the orientation had a strong influence on the growth rate, especially during anodization in oxalic acid. The electrodeposition of tin into the pores of the oxides was also studied with X-ray fluorescence and grazing-incidence transmission small-angle X-ray scattering, and it was possible to follow the increase of tin in the pores during the deposition. Generally, the method and the approach provides a tool for high statistical and temporal investigations during the growth as well as during possible applications of the nanoporous oxides, which is not obtained with standard microscopy methods that are classically used for studies of these systems.

Populärvetenskaplig sammanfattning

Aluminium och Aluminiumlegeringar, som förutom aluminium innehåller några få procent av andra metaller, används i flera olika produkter såsom mobiltelefoner, flygplan, bilar och byggnader. Bland annat är aluminiumlegeringar det mest använda byggtekniska materialet efter järnlegeringar. Det breda användandet av aluminiumlegeringar förklaras av de många fördelaktiga egenskaperna. Till exempel har legeringarna hög hållfasthet, låg vikt, hög korrosionsbeständighet och optiskt fint utseende.

Korrosion är en process som leder till att material vittrar sönder. Oftast sker detta genom att metaller reagerar med syre eller vatten som finns i den omgivande miljön och bildar tillsammans ett nytt material en så kallade oxid eller hydroxid som är en blandning av metall, syre och eventuellt väte. Ett av de kanske mest vardagliga och uppenbara problemen med korrosion är när järnmaterial på våra bilar rostar, där rost är en järnoxidhydroxid.

Aluminiummaterials höga korrosionsbeständighet kan delvis förklaras av det tunna aluminiumoxidlager som bildas direkt när aluminium kommer i kontakt med luft eller vatten. Detta lager är mycket stabilt och skyddar mot korrosion eftersom metallen inte är i direkt kontakt med omgivande miljö. På aluminium är detta naturliga oxidlager några nanometer tunt, vilket är ungefär en tiotusendel av ett hårstrå.

I mer korroderande miljöer såsom havsluft eller havsvatten behövs oftast ett förbättrat skydd. Ett sätt att öka skyddet är att producera ett tjockare oxidlager genom en elektrokemisk process som heter anodisering. Denna process utförs genom att placera aluminiummaterialet och ett annat ledande material i en ledande vätska. Därefter läggs en spänning över materialen där aluminiumet är positivt och det andra materialet är negativt. Det kommer då gå en ström från aluminiumet till det andra materialet genom oxiden och vätskan. Detta leder till oxidtillväxt på aluminiummaterialet. Oxiden som skapas kan ha olika former, vilket mestadels bestäms av vätskan som används till anodiseringen. I vätskor där oxiden är mindre lösbar bildas oftast ett jämnt lager oxid som kan bli upp till ungefär en mikrometer tjockt, vilket är ungefär som en hundradel av ett hårstrå. Om anodiseringen istället utförs i en vätska där oxiden är något löslig, vanligtvis svavelsyra, skapas en porös oxid istället. Den oxiden kan bli ännu tjockare och typiskt växer man den till 20-30 mikrometers tjocklek, vilket är en bråkdel av ett hårstrå. Denna porösa oxid har

liknande form som binas vaxkaka fast där porerna i oxiden är typiskt tiotals nanometer breda. På senare tid har det också upptäckts att för specifika anodiseringsförhållande kan porerna i den porösa oxiden organisera sig i ett mycket välordnat mönster. Detta har lett till att oxiderna också har fått mycket intresse inom nanoteknologin. Till exempel kan porerna användas som en typ av gjutningsform och fyllas med andra material.

På grund av de många applikationerna av aluminiummaterial och de anodiska oxiderna så har det utförts mycket forskning inom området. Forskningen har mestadels utförts med mikroskopi och elektrokemiska metoder. Eftersom det är svårt, speciellt med mikroskopi, att utföra mätningar med dessa metoder under oxidtillväxten eller korrosion, så är kunskapen om de bakomliggande processerna begränsade.

I denna avhandling har till stor del istället synktronljusbaserade och elektrokemiska metoder använts för att studera den naturliga och de anodiska oxiderna. Synktronljus är mycket högintensiv röntgenstrålning som fås från en forskningsfacilitet kallad synkrotron. Eftersom röntgenstrålarna vi använt oss av kan gå igenom vätskor och material, så kan man undersöka materialen när anodiseringen eller korrosionen pågår. Mestadels i detta projekt har röntgenstrålningen skjutits igenom eller låtits studsa på aluminiumoxiderna. Eftersom stålningens riktning förändras enligt formen på materialet kan man räkna ut materialets form från riktningsförändringen av strålningen. Detta har vi använt till att bestämma tjockleken av den tunna naturliga oxiden och de lite tjockare anodiska oxiderna både på rena aluminiummodellmaterial och på aluminiumlegeringar. Samtidigt som vi mäter med röntgenstrålningen har vi också genomfört elektrokemiska mätningar. Kombination av både dessa möjliggör samtida bestämningar av både formen på oxiderna och de elektrokemiska egenskaperna såsom korrosionbeständigheten.

Röntgenstrålningsmetoder användes också till att bestämma hur porerna förändras och ordnar sig under anodisering. Med metoden är det möjligt att bestämma formen på oxiden minst varje sekund. Detta är mycket snabbare än vad som är möjligt med mikroskopimetoder där anodisering behöver stoppas och mätningen måste göras i en annan miljö än anodiseringen. Det betyder att röntgenmetoden ger mycket bättre statistik över hur oxiden förändras med tiden vilket är viktigt för att få en bättre förståelse för tillväxtprocesserna.

Till sist har vi också undersökt elektrokemisk deponering av tenn i de porösa oxiderna med ordnade porer och kunde följa hur tennet fyllde porerna. Elektrokemisk deponering är en industriell använd metod för att färga in aluminiummaterial i en mängd olika färger, men även en metod för att producera nanometerstora objekt med möjliga applikationer inom nanoteknologi. Detta visar på att röntgenmetoderna och användandet av porösa oxider med ordnade porer som modeller möjliggör undersökningar av industriellt relevanta processer, men också möjliga applikationer inom nanoteknologi.

Acknowledgements

First of all, I would like to thank my supervisor, Edvin Lundgren, for all your help, guidance and support during my PhD. I am very grateful for everything I have learned, and it has been a very nice experience to work with you as my supervisor.

I would like to thank my co-supervisors, Johan Gustafson and Anders Mikkelsen, for your help and your availability to discuss any question. I would also like to thank Johan Zetterberg, Sara Blomberg and my supervisor at that time, Johan Gustafson, for all your support and help during my bachelor and master projects, which led me to continue as a PhD student at the division.

I would like to thank Florian Bertram, Gary Harlow, Nikolay Vinogradov, Lisa Rullik and Weronica Linpé for all your help with experiments, analyzing data and writing papers, and Fan Zhang and Jinshan Pan for your help with the electrochemistry. Franscesco Carlà, thank you for all help before, during and after the experiments at ESRF.

Further, I would like to thank Mikhail Shipilin, Jonas Weissenrieder, Milad Yazdi, Sarah Ahmadi, Lindsay Merte, Maria Messing, Markus Soldemo, Mats Göthelid, Jan-Olov Nilsson, Roberto Felici, and Marie Långberg for all your help during beamtimes and the help with the papers.

I would like to thank all of you at the SLJUS division for the friendly working environment. Patrik Wirgin, Anneli Nilsson Ahlm and Anne Petersson Jungbeck, thank you for all your help with economic and administrative related work.

Finally, I would like to thank my parents and the rest of my family for your understanding and support.

Preface and list of papers

This thesis present my work concerning the studies of native and anodic oxides on aluminum. The studies were performed using a combination of X-ray and electrochemical methods, where a focus is on *in situ* characterization during the electrochemical growth of the oxides. X-ray reflectivity, grazing incidence transmission small angle X-ray scattering and electrochemical impedance spectroscopy was in particular used, but also X-ray fluorescence, X-ray photoelectron spectroscopy, scanning electron microscopy and atomic force microscopy was used. Most of the experiments were performed at the large-scale synchrotron radiation facilities ESRF in Grenoble, Petra III in Hamburg, MAX IV in Lund and Diamond in Harwell.

The thesis is divided into two parts. In the first part, the materials studied and the methods used are introduced. The second part consists of the papers that present the results obtained.

Parts of this thesis has previously been presented in my licentiate thesis *"Native and Anodic Aluminum Oxides Studied by Electrochemical and Synchrotron-Based Methods"*.

The thesis is based on the following papers with my contribution described below each paper:

I F. Bertram, F. Zhang, J. Evertsson, F. Carlà, J. Pan, M. E. Messing, A. Mikkelsen, J.-O. Nilsson and E. Lundgren, *In situ anodization of aluminum surfaces studied by x-ray reflectivity and electrochemical impedance spectroscopy*, J. Appl. Phys, (2014) **116** 034902

I was involved in the measurements and discussion about the paper.

II J. Evertsson, F. Bertram, F. Zhang, L. Rullik, L. R. Merte, M. Shipilin, M. Soldemo, S. Ahmadi, N. Vinogradov, F. Carlà, J. Weissenrieder, M. Göthelid, J. Pan, A. Mikkelsen, J.-O. Nilsson and E. Lundgren, *The thickness of native oxides on aluminum alloys and single crystals"*, Appl. Surf. Sci. (2015) **349** 826-832

I was involved in the planning and took part in the measurements. I analyzed the data and wrote the manuscript.

III F. Zhang, J. Evertsson, F. Bertram, L. Rullik, F. Carlà, M. Långberg, E. Lundgren and J. Pan, *"Integration of electrochemical and synchrotron-based X-ray techniques for in-situ investigation of aluminum anodization"*, Electrochim. Acta **241** (2017) 299–308

I was involved in the planning of the experiments, analyzed parts of the data and wrote parts of the paper.

IV J. Evertsson, F. Bertram, L. Rullik, G. Harlow and E. Lundgren, *"Anodization of Al(100), Al(111) and Al Alloy 6063 studied in situ with X-ray reflectivity and electrochemical impedance spectroscopy"*, J. Electroanal. Chem., **799** (2017) 556–562
I was responsible for the planning and performing the experiments. I analyzed the data and wrote the manuscript.

V N. Vinogradov, G. S. Harlow, F. Carlà, J. Evertsson, L. Rullik, W. Linpé, R. Felici and E. Lundgren, *"The growth and self-organisation of anodic alumina nanopores studied by time resolved X-ray scattering,* In manuscript

I was involved in the measurements and took part in the discussion about the manuscript.

VI J. Evertsson, N. A. Vinogradov, G. S. Harlow, F. Carlà, L. Rullik, W. Linpé, R. Felici and E. Lundgren*, "Self-organization of nanoporous aluminum oxides studied in situ with grazing-incidence transmission small-angle X-ray scattering"*, In manuscript

I was involved in the planning and took part in the measurements. I analyzed the data and wrote the main parts of the manuscript.

VII W. Linpe, G. S. Harlow, J. Evertsson, U. Hejral, F. Lenrick, S. Siefert, R. Felici, N. Vinogradov and E. Lundgren, *"In-situ X-ray observations of Sn electrodeposition into two-step anodized alumina"*, In manuscript.

I was involved in the measurements and took part in the discussion about the manuscript.

Papers that are not included in the thesis, to which I have contributed

VIII J. Zetterberg, S. Blomberg, J. Gustafson, J. Evertsson, J. Zhou, E. C. Adams, P.-A. Carlsson, M. Aldén and E. Lundgren, *Spatially and temporally resolved gas distributions around heterogeneous catalysts using infrared planar laser-induced fluorescence*, Nat. Commun. (2015) **6** 7076

IX C. Zhang, J. Gustafson, L. R. Merte, J. Evertsson, K. Norén, S. Carlson, H. Svensson and P.-A. Carlsson, *An in situ sample environment reaction cell for spatially resolved x-ray absorption spectroscopy studies of powders and small structured reactors*, (2015) **86** 033112

X E. C. Adams, L. R. Merte, A. Hellman, M. Skoglundh, J. Gustafson, E. C. Bendixen, P. Gabrielsson, F. Bertram, J. Evertsson, C. Zhang, S. Carlson and P.-A. Carlsson, *The structure–function relationship for alumina supported platinum during the formation of ammonia from nitrogen oxide and hydrogen in the presence of oxygen*, Phys. Chem. Chem. Phys., 2016, **18**, 10850-10855

XI L. Rullik, F. Bertram, Y. R. Niu, J. Evertsson, T. Stenqvist, A. A. Zakharov, A. Mikkelsen and E. Lundgren, *Surface Development of an Aluminum Brazing Sheet during Heating Studied by XPEEM and XPS*, Mater. Res. Express **3** 106506 (2016)

XII L. Rullik, N. Johansson, F. Bertram, J. Evertsson, T. Stenqvist, E. Lundgren, *"Surface development of a brazing alloy during heat treatment - A comparison between UHV and APXPS"*, In press.

XIII J. Kiefer, J. Zetterberg, A. Ehn, J. Evertsson, G. Harlow, E. Lundgren *Infrared Spectroscopy as Molecular Probe of the Macroscopic Metal-Liquid Interface*, In press.

List of abbreviations

AA	Aluminum alloy
AFM	Atomic force microscopy
ALD	Atomic layer deposition
ALUX	ALUminium oXides for processing and products
AR	Anodizing ratio
CE	Counter electrode
CPE	Constant phase element
CV	Cyclic voltammetry
CVD	Chemical vapor deposition
ECD	Electrochemical deposition
EIS	Electrochemical impedance spectroscopy
FCC	Face-centered cubic
GISAXS	Grazing-incidence small-angle X-ray scattering
GTSAXS	Grazing-incidence transmission small-angle X-ray scattering
LTO	Low-temperature oxidation
NP-AAO	Nanoporous anodic aluminum oxide
OCP	Open-circuit potential
PEEK	Polyether ether ketone
PVD	Physical vapor deposition
RE	Reference electrode
SAXS	Small-angle X-ray scattering
SEM	Scanning electron microscopy
WE	Working electrode

WAXS	Wide-angle X-ray scattering
XPS	X-ray photoelectron spectroscopy
XRD	X-ray diffraction
XRF	X-ray fluorescence
XRR	X-ray reflectivity

Contents

1 Introduction

Aluminum and aluminum alloys are extremely important materials that are found in a broad range of products such as electronic devices, vehicles, air planes and buildings [1]. After ferrous metals, aluminum alloys are the most used material in structural engineering [2]. Aluminum materials are used due to its high strength to weight ratio, hardness, corrosion resistance and optically attractive oxidized surface that is also possible to obtain in a diverse range of colors [1, 3, 4].

The corrosion resistance properties rely in many situations on an alumina film that is formed on the surface and that protects the metal from the surrounding environment. In room temperature and air, a thin native alumina film (2-7 nm) is formed naturally on aluminum [3, 5-7]. This film provides the material with protection against corrosion in many environments. Nevertheless, in harsher outdoor environments such as seawater that contain aggressive chemicals, this thin film is not enough and local corrosion can still occur, especially on aluminum alloys [1]. A way of increasing the protection and make the material also suitable for harsher environments is to increase the oxide film thickness electrochemically by a process called anodization. The process has been known for very long time and was already in the 1920s used industrially to increase the corrosion resistance of aluminum products such as seaplane parts [1]. The anodic oxide film can have two different morphologies, barrier- or porous-type. Whereas the barrier-type oxide is more of a homogeneous layer, the porous-type oxide film contains mutually parallel nanometer-sized pores that extend through almost the entire oxide.

More recently, in 1995, it was presented that under specific electrochemical conditions the pores can self-organize during anodization [8, 9]. The pores in these ordered nanoporous aluminum anodic oxides (NP-AAO) have the same size and are organized in a hexagonal close-packed arrangement. These ordered structures have already found applications in nanotechnology, such as for synthesizing nanostructures, and have in the future been proposed to be used for functional nanodevices [10-13].

Aluminum oxides have due to its importance received enormous attention in both fundamental and applied research. The structure and growth mechanism of very thin aluminum oxides have been studied with surface science techniques in highly controlled ultra-high vacuum conditions [14-29] as well as by theoretical means and are known to a high degree [30, 31]. Also, the structure of crystalline bulk aluminum

oxides and hydroxides formed at higher temperatures have in much been determined [32-35].

Even if aluminum oxides formed at low temperatures and by anodization have been studied extensively in the past, the structure and growth mechanism is not fully known due to their amorphous structure, insulating nature, complex composition and growth environments where for example traditional *in situ* electron-based techniques are not possible to use due to the short mean free path of electrons in liquids.

Instead, these oxides have mainly been studied by electrochemical means and using microscopy methods [4, 36-39]. From these studies, many empirical relationships have been established between the growth conditions and the properties of the produced oxide on both pure aluminum and aluminum alloys. These methods have also been used to investigate corrosion of aluminum materials where the effect of the oxides and the alloying elements on the protection have been studied [40-43].

Although many of the mechanisms have been explained, there are still important details that are debated. Hence, to improve the understanding of the mechanisms and pave the way towards a more rational development, the oxides and realistic aluminum alloys need to be studied *in situ* during anodization and corrosion in relevant environments [1].

To realize this, methods based on a probe that can penetrate through an electrochemical cell, the electrolyte and even the oxide and the aluminum itself is needed to be used. These demands are satisfied by methods based on hard X-rays, such as X-ray diffraction (XRD), X-ray reflectivity (XRR) and small-angle X-ray scattering (SAXS). In the literature, there are several examples where these methods have been used successfully to study both catalytic and electrochemical systems at realistic or near realistic conditions, see for example [44-51].

In the present thesis, the main focus is to present the studies of the growth and stability of native and anodic oxides on pure aluminum single crystals and polycrystalline substrates as well as on realistic industrial aluminum alloy substrates. A large part of the work has been to integrate traditionally used electrochemical methods with synchrotron-based scattering techniques enabling the use of this combination simultaneously. The combination provides a unique possibility of *in situ* studies of both structural and electrochemical properties during realistic electrochemical processes such as anodization and corrosion. Studies performed on substrates with a large range of complexity is important as it can provide information regarding the relevance of the results obtained from model substrates for the realistic materials.

This PhD project has been a part of the SSF-Program *ALUminium oXides for processing and products* (ALUX) [52]. The program is a collaboration between Swedish academia and aluminum industry with expertise in novel experimental *in situ* techniques and theory. The goal of the project is to improve the understanding of corrosion and anodization of relevant aluminum materials, with the ultimate goal to increase the corrosion resistance and versatility of aluminum products.

2 Aluminum and aluminum alloys

In the present thesis, native and anodic aluminum oxides have been studied on substrates ranging from fundamental surface science-friendly model aluminum single crystal surfaces to realistic industrial polycrystalline aluminum alloys, which are used in a large variety of applications today.

The low complexity and well-defined chemical nature of low index surfaces and single crystal surfaces in general, facilitate fundamental research since it is easier to determine the reason for an occurring event when the possibilities are fewer. This is not the case for polycrystalline surfaces, where all possible orientations can co-exist on the same substrate, and especially not for industrial aluminum alloy surfaces, where also other elements further increase the complexity.

Nevertheless, it is important to perform studies on substrates with a diverse range of complexity to be able to determine if and to what degree the results obtained on model substrates are also possible to apply on realistic materials.

In the following sections, the single crystals (section 2.1), polycrystalline aluminum and industrial aluminum alloys (section 2.2) substrates will be described. Afterwards, the importance of surfaces is introduced (section 2.3).

2.1 Single crystals

In a single crystal, the atoms or groups of atoms are arranged in a three-dimensional periodic array. To describe this structure the concepts of basis and lattice are used [53]. A basis is a group of atoms that are positioned at periodic points of an infinite lattice. The lattice is described by three translation vectors $\boldsymbol{a}_1$, $\boldsymbol{a}_2$ and $\boldsymbol{a}_3$ such that the atomic arrangement looks the same for all translations from a point in the lattice to all other points defined by integer multiplies of $\boldsymbol{a}$'s. Mathematically the lattice is defined by the set of points described by $\boldsymbol{R} = m_1\boldsymbol{a}_1 + m_2\boldsymbol{a}_2 + m_3\boldsymbol{a}_3$, where m_1, m_2 and m_3 are integers. The position of the atoms j that constitutes the basis are defined relative to the lattice point,

$$\boldsymbol{r}_j = x_j\boldsymbol{a}_1 + y_j\boldsymbol{a}_2 + z_j\boldsymbol{a}_3 \tag{2.1}$$

where x_j, y_j and z_j are between 0 and 1.

Different lattices are described by the concepts of conventional unit cells. A cell is a volume, including atoms that with a suitable translation will fill the entire space and describe the lattice. The atoms in Al is arranged according to the face-centered cubic (fcc) lattice, which conventional cell is shown in Figure 2.1. The cell consists of a ¼ atom in each corner (red) and ½ atom at each face (blue). A cell is defined by its lattice parameters (a, b, c) and the angles (α, β, γ) between the axes. For the Al fcc cell is $a = b = c = 4.05$ Å and $\alpha = \beta = \gamma = 90°$.

In surface science, the surfaces of crystals are denoted according to the plane at which the crystal has been cut to expose the surface. The Miller indices are the conventional way of defining planes of crystals and surface orientations. A plane is determined by the reciprocals of the interceptions between the plane and the coordinate axes. The combination of the numbers reduced to the smallest integer combination with the same ratio is called the index of the plane and is written as (hkl), where h, k, l are integers. Figure 2.1 (a-c) show the three low index planes in the cell of the fcc lattice with their corresponding indices indicated. Below each cell are also the corresponding surfaces that are obtained by cutting the crystal according to the planes shown in the cells above. Downwards from the surface is an atomic layer repeated every second layer for (100) and (110) and every third layer for the (111) surface.

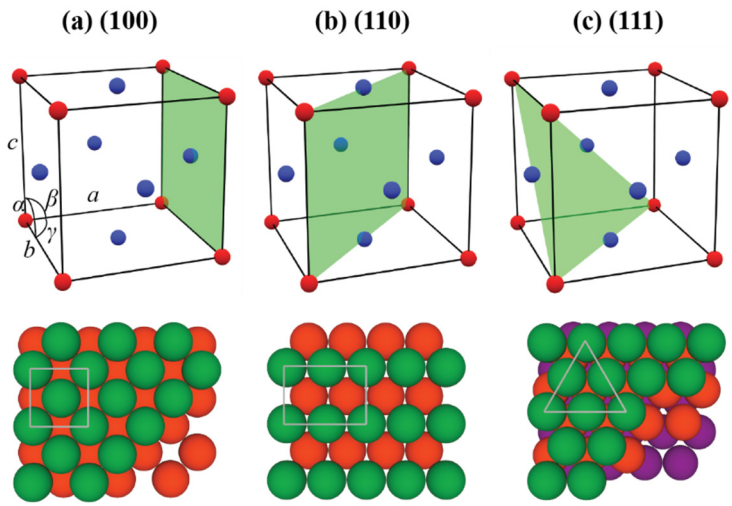

Figure 2.1: Illustration of the fcc lattice conventional cell with three low-index planes in the cell indicated by the green areas. In cell (a) the lattice parameters (a, b, c) and the angles (α, β, γ) betweens the axes are shown. For the fcc cell is $a = b = c$ and $\alpha = \beta = \gamma = 90°$. Below each cell is the corresponding surface of a crystal that are cut according to the plane. The grey square, rectangle and triangle corresponds to the green area in the cells.

2.2 Polycrystalline aluminum and aluminum alloys

A step up from single crystals in complexity are polycrystalline materials. These consist of many smaller crystalline grains that are orientated randomly to each other. The random grains and the boundaries between the grains provide the material with other mechanical, oxidation and corrosion properties than a single crystal. The size of the grains in polycrystalline Al is typically between a few µm up to several mm, which is determined by how the material has been treated. The surface of polycrystalline materials is more complex than a single crystal surface since it can have all types of crystal surface orientations exposed on the same surface with grain boundaries in between.

The most complex material studied during the project were commercial industrial or wrought aluminum alloys (AA). AA is formed by adding different amounts of other elements to aluminum when in the molten state. The properties of the formed AA are further modified by mechanical and heat treatments. The final material consists of larger grains (usually hundreds of micrometers [54]) with a more general alloy matrix metal composition, but also different types of smaller (Å-10 µm) intermetallic particles that have different composition and chemical properties [2].

The main reason for adding alloying elements is to improve the mechanical properties of the material, but the elements also introduce heterogeneities into the microstructure that have radical implications on both the corrosion resistance and formed anodic oxides [2], see section (3.1.1.1) and (3.2.4), respectively.

Table 2.1 shows the composition of the AA studied in this thesis, where the total amount of alloying elements are between about a few to 10 wt. %. Every AA is designated with a number where the first number is determined by the main alloying element in the AA. The main alloying elements in 6### series are Si and Mg, and in 7###, the main elements are Zn and Mg.

Table 2.1. The chemical composition of the Aluminum Alloys studied in the project. [wt.%.]. The remainder is Al. [55]

Sample	**Si**	**Fe**	**Cu**	**Mn**	**Mg**	**Cr**	**Zn**	**Ti**
AA 6005	0.50–0.90	0.35	0.30	0.50	0.40–0.70	0.30	0.20	0.10
AA 6060	0.30–0.60	0.10–0.30	0.10	0.10	0.35–0.60	0.05	0.15	0.10
AA 6063	0.20–0.60	0.35	0.10	0.10	0.45–0.90	0.10	0.10	0.10
AA 6082	0.7–1.3	0.50	0.10	0.40–1.0	0.60–1.2	0.25	0.20	0.10
AA 7075	0.40	0.50	1.2–2.0	0.30	2.1–2.9	0.18–0.28	5.1–6.1	0.20

To be able to study the polycrystalline and AA substrates using surface sensitive X-ray scattering techniques and facilitate the comparison with single crystal surfaces, the surface was polished to a roughness level close to that of the single crystal surfaces. In particular, for XRR extremely flat surfaces are needed. Figure 2.2 illustrates how the AA substrates were made, which begins with commercial extrusion profile (a) from which mm in diameter sized disc (b) were cut out and then mechanically polished (c).

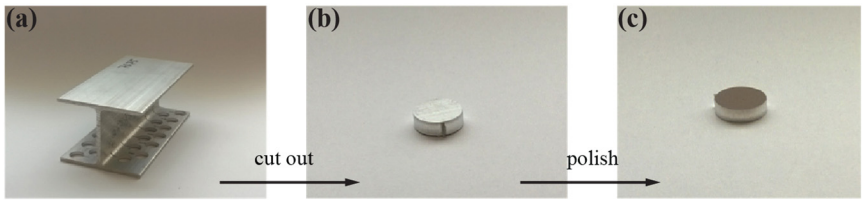

Figure 2.2: Photos illustrating the aluminum alloy substrate preparation. The sample is cut from extruded aluminum profiles (a) into 5-10 mm diameter round discs (b). They are then polished to a mirror-like finish with a roughness of less than 0.03 μm (c).

2.3 Surfaces

The atoms at the surface of a material have higher energy than compared to the energy of the atoms in the bulk of the material since the amount of neighboring atoms and the bonds between them is less at the surface than in bulk. Hence, there is a tendency towards minimizing this surface energy, which can occur in different ways. For polycrystalline surfaces, the grains can be orientated such that denser surfaces face the environment. The atoms of more open surfaces where the distance between atoms is long such as fcc(110) can reconstruct to a more close-packed arrangement. For AA elements can segregate to and from the surface.

In addition to these more intrinsic processes, the surface energy can also be lowered by the adsorption of species from the environment such as O_2 and H_2O. For most metals including Al the adsorption can further result in the dissociation of the adsorbed species, and if the energy gain is high enough the oxygen can mix with the metal resulting in the formation of an oxide between the metal and environment. The surface of aluminum is very reactive, and oxides are formed very easy. For example at room temperature at a pressure of 10^{-7} mbar of either O_2 and H_2O a couple of Å thick oxide film is formed in hours and at atmospheric pressures nm thick oxide film is formed within at least minutes [23, 31]. For aluminum alloys, oxidizing environments can also result in the migration and oxidation of elements as they have different affinities to oxygen.

To conclude, most materials interact with the environment with their surfaces. The properties and composition of the surface region are different from that in the bulk and can also change during processes such as corrosion and oxidation. Hence, it is important to specifically probe and study the surface region instead of the entire sample including the bulk. Further, as the surface region changes due to the occurring processes, *in situ* studies are essential.

3 Electrochemistry and aluminum oxide structures

In electrochemistry, the relationships between electrical currents and electrochemical reactions are studied. The field of electrochemistry began with the invention of a sustainable electrical source, the battery, in 1800 by Alessandro Volta. Soon after, Michael Faraday, defined the concepts of anode, cathode, electrode, electrolyte and ion, which definitions are the cornerstone of the field of electrochemistry [56].

Electrochemistry is used today extensively both in fundamental research and in mature applied chemical processes [56]. Anodization, which was studied in the present thesis, and corrosion are two example of electrochemical processes. Also, the electrochemical method, electrochemical impedance spectroscopy (EIS), was used in the present thesis.

The following sections will first introduce electrochemical cells (section 3.1) and corrosion (section 3.1.1). In the final section native and anodic oxides are described (section 3.2).

3.1 Electrochemical cells

Figure 3.1 shows two examples of electrochemical cells, i.e. (a) electrolytic and (b) corrosion cell, which is a type of galvanic cell. The cells consist of two half-cells where each half-cell includes an electrode in an electrolyte. The two half-cells can use the same electrolyte or different electrolytes kept apart by for example a membrane, that still allows ions to be transported between the half cells. The electrodes are also connected by a metallic conductor in which electrons can move.

At one of the electrodes (anode), an oxidation reaction (loss of electrons) occurs at the interface, and a reduction reaction (gain of electrons) occurs at the interface of the other electrode (cathode). In the case of an electrolytic cell, an external power supply determines which electrode that becomes the anode and cathode. For a

galvanic cell, it is instead the nobility of the material that determines the nature of the electrode, where a less noble material will be the anode.

The reactions at the electrode interfaces result in a change of the amount of ions in the electrolyte close to the electrodes, and also in the number electrons available from the electrodes. Hence, these half-reactions are coupled by the transport of electrons through the metallic conductor and ions through the electrolyte that neutralizes the charge difference and allows for the continuation of the reactions, which otherwise would have stopped due to the buildup of charge close to the electrodes. The transport of ions does not need to only consist of the ions formed by the reactions, but can also be other ions existing in the electrolyte.

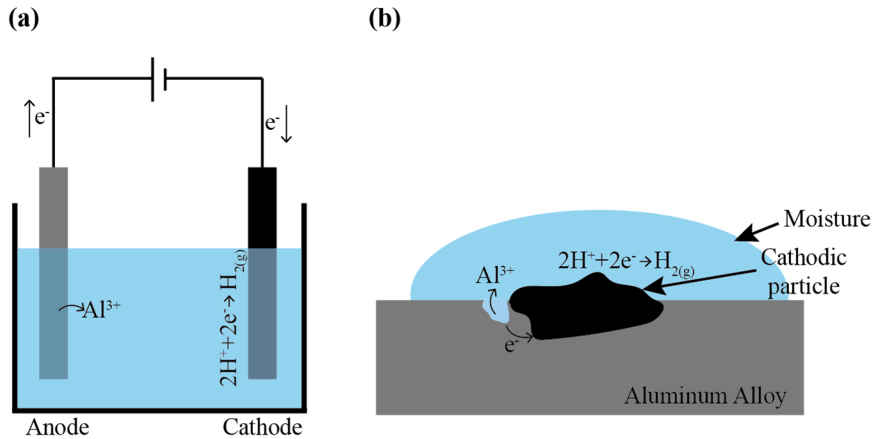

Figure 3.1: (a) Simplified illustration of an electrolytic cell during anodization of aluminum. (b) Simplified illustration of a corrosion cell or galvanic cell during corrosion of an aluminum alloy. In the corrosion cell shown, the aluminum alloy matrix is the anode and also allowing electrons to pass between the anodic and cathodic regions.

The current can be measured in the metallic conductor and used to analyze the reactions occurring in the cell as well as the properties of the interfaces between the electrode and electrolyte.

In addition to anode and cathode, the electrodes can also be defined according to their use in the cell, i.e. working electrode (WE), reference electrode (RE) and counter electrode (CE). The WE is usually the electrode that is of interest, which means that measured changes should correspond to changes at this electrode. This is accomplished in a two electrode setup by using a combined RE/CE that are stable enough and does not change significantly due to the reaction occurring. If higher accuracy is needed, a three-electrode setup can be used instead. In this setup, the RE and CE are two different electrodes. The potential of the RE is stable when only minor reactions occur and are used as a reference for setting the potential of the WE.

The stability of the RE is satisfied due to its high impedance such that most of the current passes through the WE and CE [57].

3.1.1 Corrosion

Corrosion is defined as the deterioration process of materials by an electrochemical process and is the result of the simultaneous transfer of charge and mass across a material/electrolyte interface [58]. Even if all materials corrode to some extent, only metals are usually considered for corrosion. Corrosion occurs spontaneously in natural environments and deteriorates metals by converting the material towards more oxidized phases.

The process of corrosion occurs in a corrosion cell (see Figure 3.1 (b)), which is a kind of galvanic cell. The anode and cathode in the cell are two different regions in the metal that are in metallic contact through the material itself, and the electrolyte can be a thin film of moisture. The possibility that a region can act as an anode and another region as a cathode is due to the heterogeneous nature of metals. In pure metals, areas with higher total energy or less noble regions can act as the anode and can, for example, be crystal orientations with higher surface energies, grain boundaries, steps, kinks and stressed regions. In metal alloys also regions with different compositions can acts as either anodic or cathodic compared to the general alloy matrix where one example is intermetallic particles.

For corrosion, the anodic reaction results in the loss of metal, and for Al the reaction is

$$\mathrm{Al(s)} \rightarrow \mathrm{Al^{3+}(aq)} + 3\mathrm{e^-} \tag{3.1}$$

and the cathodic reactions are oxygen reduction

$$\mathrm{O_2} + 2\mathrm{H_2O} + 4\mathrm{e^-} \rightarrow 4\mathrm{OH^-} \tag{3.2}$$

and hydrogen reduction

$$2\mathrm{H^+} + 2\mathrm{e^-} \rightarrow \mathrm{H_2} \tag{3.3}$$

where the oxygen reduction occurs in more neutral and basic solutions, and hydrogen reduction in more acidic solutions [58].

3.1.1.1 Corrosion of aluminum and aluminum Alloys

Aluminum alloys (AA) and especially pure Al are considered to have good corrosion resistance in neutral environments, due to the non-conducting alumina film that naturally exists on the materials, and that is self-repaired if damaged [2]. However, in environments with a pH that is not neutral, the alumina film is soluble,

and it becomes possible for the environment to reach the metal locally. This results in localized pitting corrosion of the metal at regions where the alumina film has been weakened. The alumina film can also be weakened by aggressive anions such as Cl^- ions, a process which is still under debate but possibly due to the formation of soluble complexes with surface Al ions at the alumina film surface [2, 59, 60].

The lower corrosion resistance of AA is related to the higher amount of heterogeneities of the material introduced by the alloying elements in the size of a few Å to 10 μm intermetallic particles [2]. These particles can be of either anodic or cathodic type compared to the alloy matrix and hence either be dissolved (anodic type) or lead to the dissolution of the aluminum around the particle (cathodic type). The lower corrosion resistance of AA is also aided by a possible weaker alumina film close the intermetallic particles.

There exist several methods to increase the corrosion protection of aluminum materials, for example by reducing the amount of intermetallic particles or other heterogeneities, or by producing more protective coatings than the native alumina film on the material. Anodic oxide films produced by anodization is one method of coating used to increase the corrosion resistance of aluminum-based materials.

3.2 Native and anodic aluminum oxides films

Figure 3.2 illustrates the three types of aluminum oxide films that were studied in the present thesis. Figure 3.2 (a) is a native oxide film that is formed spontaneously at room temperature in air. Figure 3.2 (b) and (c) illustrate anodic barrier-type and porous-type oxide films that are formed in neutral and acidic electrolytes during anodization, respectively. In the following, the structure and composition of these oxides (3.2.1), the characteristics and growth theory of native (3.2.2) and anodic (3.2.3) oxides and the effect of alloying elements (3.2.4) will be introduced. Extensive reviews regarding these subjects can be found in for example refs. [1, 3, 7, 61, 62].

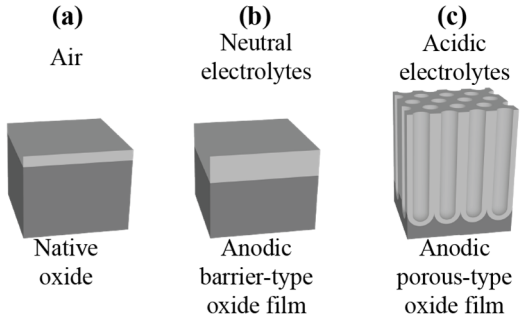

Figure 3.2: Illustrations of the three oxide films studied in the present thesis. (a) Native oxide films are formed in air and at room temperature. (b) Anodic barrier-type oxide films are formed in neutral electrolytes during anodization. (c) Anodic porous-type oxide films are formed in acidic electrolytes during anodization.

3.2.1 Structure and composition

The structure and composition of as prepared native and anodic aluminum oxides are complex and varies with the formation conditions. The structure is commonly described as amorphous, with possible crystalline patches, and is similar to γ-Al_2O_3 (gamma-alumina), see Figure 3.3 (a). Also, hydroxides such as boehmite (γ-AlOOH) and bayerite (α-$Al(OH)_3$) have been considered, see Figure 3.3 (b) and (c), respectively [3, 61].

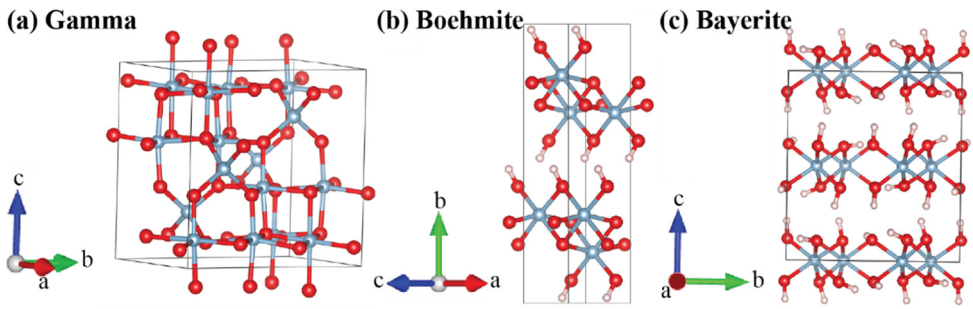

Figure 3.3: Illustration of (a) γ-Al_2O_3 (Gamma-alumina), (b) γ-AlOOH (Boehmite), (c) α-$Al(OH)_3$ (Bayerite). Oxygen atoms are represented by red, aluminum atoms by blue and hydrogen by white spheres. Lattice parameters for (a) γ-Al_2O_3: $a = 5.587$ Å, $b = 8.413$ Å, $c = 8.068$ Å and $\beta = 90.59°$, (b) γ-AlOOH: a = 2.876 Å, b = 12.240 Å and c = 3.709 Å, (c) α-$Al(OH)_3$: $a = 5.063$ Å, $b = 8.672$ Å, $c = 9.425$ Å and $\beta = 90.26°$. Drawing produced by VESTA [63] using coordinates in ref. [33, 34].

It has also been determined that in addition to 4- and 6-fold coordinated Al, which are the only building blocks in crystalline γ-Al_2O_3, also 5-fold coordinated Al with

O exist in anodic oxides [64, 65]. The 6-, 5- and 4-fold coordinated building blocks are illustrated in Figure 3.4 (a), (b) and (c), respectively. The amount of each coordination varies with the electrolyte in which the anodization is performed [64], and these variations have been proposed to be related to the incorporation of anions, hydrogen and water in the oxide [1, 64].

The incorporation of anions, such as SO_4^{2-}, from the electrolyte occurs by inwards migration due to the electric field. This affects the porous-type oxides more than the barrier-type oxides and results in a double type of pore walls with an anion incorporated outer layer and a relatively pure inner layer [3]. The barrier-type oxide has a relatively pure inner layer and anion incorporated outer layer next to the oxide/electrolyte interface. These incorporated electrolyte species act as doping and can alter the dielectric, conductivity, electric field profile, chemical and mechanical properties of the oxide. This in turn can affect the limiting thickness, growth rate and corrosion as well as the self-organization of the pores in porous-type oxides [61, 66-69].

To conclude, the structure and composition of these oxides is not homogeneous and is not very well defined. This has complications for several electrochemical methods, such as electrochemical impedance spectroscopy, and X-ray photoelectron spectroscopy. For example to determine thicknesses using these methods the density and/or the dielectric constant is needed to be known. If that is not the case, the uncertainty in the determined values will be high due to the large range of values the density (2.7-3.5 g/cm^3) and dielectric constant (7.5-15) can possess [70-74].

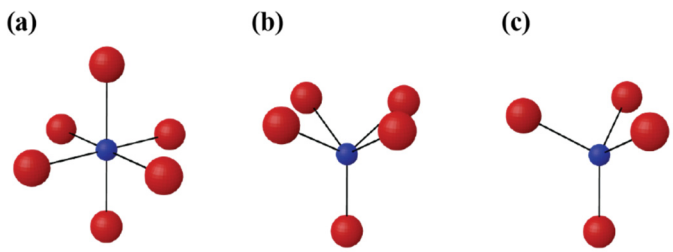

Figure 3.4: Illustrations of (a) Octahedral (AlO_6), (b) Tetrahedral (AlO_5) and (c) Pyramidal (AlO_4) building blocks of aluminum oxides. Blue spheres are Al atoms, and red spheres are O atoms.

3.2.2 Native oxide films

Due to the high affinity of aluminum to oxygen, an amorphous alumina film is formed on most aluminum materials in oxidizing environments [3]. At atmospheric pressures and low temperatures, i.e. room temperature, a self-limiting 2-7 nm thick

native oxide film is formed on the material in air, oxygen and water [6, 7, 74]. Since the oxide acts as a passivating layer between the metal and the environment and since the film is self-renewed by re-oxidation after damage, the oxide also provides aluminum-based materials good corrosion resistance in many environments [1].

The growth of native oxides such as alumina on aluminum follows the low-temperature oxidation (LTO) process that was explained by Cabrera and Mott [6, 7]. In their model, electrons from the Al metal traverse the growing oxide film and ionizes oxygen-containing species at the oxide/environment interface. The positive Al ions at the Al/oxide interface and the negative oxygen-containing ions at the oxide/environment interface generates a so-called Mott potential that is approximately stable during the whole growth process. The resulting field across the oxide decreases the barrier for ions sufficiently such that transport of ions through the oxide is possible. This field supported transport is explained by a hopping mechanism, where the ions jump from regular sites or interstitial positions to neighboring vacancies or interstitial sites [61]. The ions that are transported through the oxide react with its counterpart at the other interface and form new oxide. The transport and oxide growth is high in the beginning when the oxide is thin, and the electric field strength is high, but as the oxide film grows thicker the electric field strength decreases and as consequence also the growth rate decreases. When the electric field strength is low enough, the barrier is too high for ionic transport to proceed and as a result, the oxide stops growing. This theory successfully explains both the growth process and the reason for the limited oxide thickness. However, the limited thickness has from theoretical calculation also been attributed to a decrease in adsorption energy of oxygen molecules with increasing oxide thickness [31]. This influences both the oxygen supply needed for oxide formation and the Mott potential needed for the transport.

3.2.3 Anodization and anodic oxide films

In corrosive environments (e.g. seawater, chlorides or sulfates), the protection that the native oxide provides aluminum materials is usually not sufficient and local corrosion can occur [1]. A common method to increase the protection is to grow a thicker anodic oxide electrochemically by anodization. This method has been exploited for almost a century and is today extensively used industrially [1]. Besides the increased corrosion resistance, the anodic oxides provide excellent hardness and abrasion resistance [3]. The anodic oxide is also viewed as optically attractive both in its natural appearance and after coloring with for example electrolytic deposition techniques [3]. Anodized aluminum can today be found in electronic devices, cookware, outdoor products, plasma equipment, vehicles, airplanes, architectural materials and much more [1]. More recently, much attention has been directed

towards self-ordered periodic nanoporous anodic oxides, which is a highly promising material for nanotechnological applications [1, 8, 9, 75].

The properties of anodic oxides and the processes occurring during anodization have been studied extensively and been explained in detail. Especially the empirical relations between the conditions during anodization and the final produced material is known to a high degree. However, even if there is a significant knowledge on empirical aspects, a full understanding of atomistic processes is lacking and highly debated.

Figure 3.5 shows an illustration of anodization of aluminum with some possible key reactions occurring during the process indicated [1, 69]. The anodization is performed in an electrolytic cell where the Al is the anode, and another conducting and sufficiently stable material is the cathode. The potential difference can be kept constant (potentiostatic mode) or varied to keep the current constant (galvanostatic mode) during the process. While anodizing reactions (R1-R8) occur at the anode, hydrogen evolves at the cathode (R9). The reactions at the anode occur at the oxide/electrolyte and Al/oxide interfaces. At the oxide/electrolyte interface water is heterolytic dissociated (R1) and the formed O^{2-}, OH^{-} anions can take part in oxide formation (R2), oxygen formation (R3) or be transported towards the Al/oxide interface.

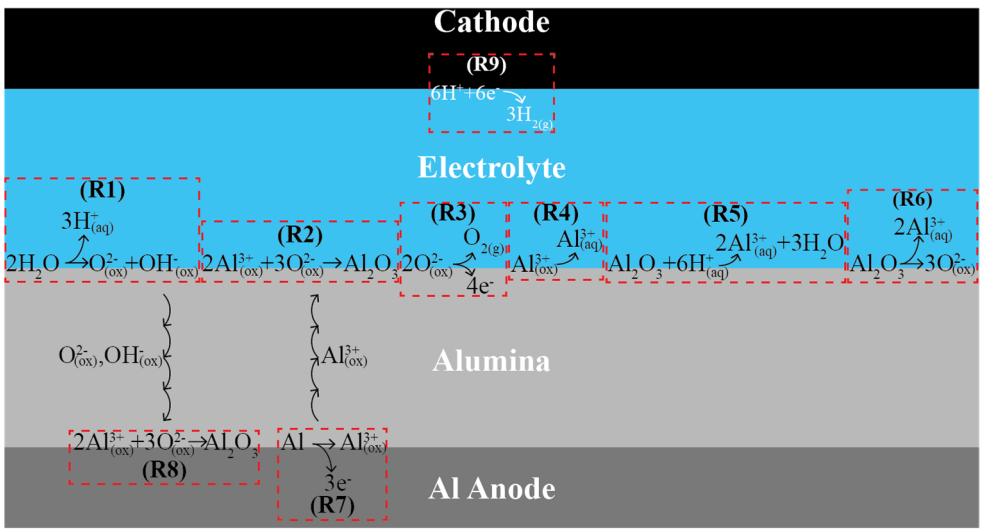

Figure 3.5: Illustration of anodization of aluminum with some key reaction occurring during the process. ox: oxide; aq: aqueous; g: gas.

This transport follows the same hopping mechanism as for the native oxide growth described in section (3.2.2) [61]. Also at the oxide/electrolyte interface, transported Al^{3+} cations can, instead of taking part in oxide formation with O^{2-}/OH^{-}, be

directly ejected into the electrolyte (R4) and oxide can be dissolved (R5) or decomposed (R6). At the metal/oxide interface the Al can be ionized (R7), and the formed Al^{3+} cations can be either transported towards the oxide/electrolyte interface or form oxide by reacting with O^{2-}/OH^{-} anions (R8). If all the cations and anions takes part in oxide formation, i.e. only reaction (R1-R2, R7-R8) occurs, the overall reaction at the anode will be

$$2Al(s) + 3H_2O(l) \rightarrow Al_2O_3(s) + 6H^+ + 6e^- \quad (3.4)$$

This is, however, seldom the case and it is always expected that some Al^{3+} cations are directly ejected, and some alumina is dissolved or decomposed for all anodization conditions. The amount of ejected Al^{3+} cations can be measured by placing an immobile marker in the native oxide before the anodization begins as shown in Figure 3.6 (a). If all Al^{3+} ions transported to the oxide/electrolyte interface takes part in oxide formation the marker level will be found at 40 % of the total thickness, see Figure 3.6 (b). If all the Al^{3+} ions instead are ejected into the solution no oxide is formed at the oxide/electrolyte interface and the marker level can be found at the surface, see Figure 3.6 (c). Figure 3.6 (b-c) is representative for the extreme cases of barrier-type oxide films, and also cases in between these two can occur. For porous-type oxide films, the Al^{3+} ions are always ejected into the solution, and the marker level can be found on the surface of the oxide, see Figure 3.6 (d).

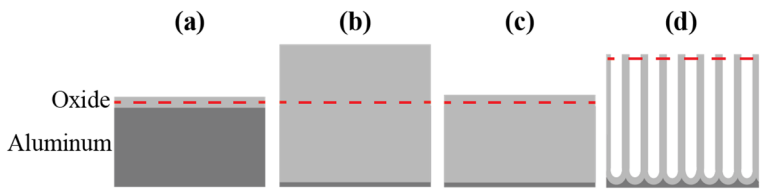

Figure 3.6: Immobile marker level experiment showing the effect of different amount of ejected Al^{3+} ions into the electrolyte during anodization. (a) Marker level as implemented into the native oxide. The result (b) when all Al^{3+} ions transported to the oxide/electrolyte interface takes part in oxide growth, (c) when all Al^{3+} ions are instead ejected into solution and oxide mainly grows at the Al/oxide interface. (d) For porous-type oxides all Al^{3+} ions are ejected into the solution. Adapted from [37].

The morphology of the growing oxide mostly depends on the electrolyte used during the anodization. In more neutral electrolytes where the oxide is generally not soluble a compact, and nonporous barrier-type oxide film is often formed. In more acidic electrolytes, where the oxide is partly soluble porous-type oxide films are formed. During anodization, one way to determine if a barrier- or porous-type oxide film is formed is to study the current that passes through the cell, see Figure 3.7. When using a constant anodization potential, the current decreases almost exponentially with time (blue) when barrier-type oxide films are formed, whereas when porous-

type oxide films are formed the current increases again after a minimum have been reached and finally levels out at a higher value than for barrier-type oxide films. The following sections will further introduce the properties and growth characteristics of barrier-type oxide films (3.2.3.1) and porous-type oxide films (3.2.3.2).

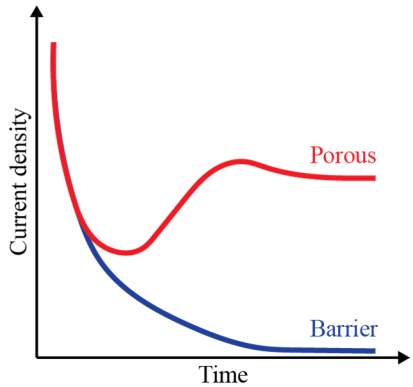

Figure 3.7: Typical current transients during growth of barrier- and porous-type oxide films under potentiostatic mode. Adapted from [3].

3.2.3.1 Barrier-type oxide films

As mentioned above barrier-type oxide films are possible to form in neutral electrolytes (pH 5-7) where the oxide is generally not soluble [1, 3]. The electrolyte should preferably also have a pH buffer capacity as the anodization reactions can lower the pH of the electrolyte. Common electrolytes used are borate, oxalate, citrate, phosphate, adipate and tungstate solutions [1].

The oxide films formed on flat and pure aluminum substrates are generally considered to be homogeneous with uniform height and flat interfaces. The thickness of the oxide films can be as high as 1 µm and are directly proportional to the anodization potential. The proportionality to the potential is commonly called the anodizing ratio (AR), which is about 1.4 nm/V for compact aluminum barrier-type oxide films [1, 3].

The exponentially decreasing current measured during the formation of barrier-type oxide films as shown in Figure 3.7 is mainly due to the ionic current through the oxide. The other component is a small electronic contribution due to the transport of electrons through the oxide [3]. The empirical obtained relationship of the ionic current density under high electric field has been established as

$$j_{ion} = A\exp(BE) = A\exp\left(\frac{BU_{ox}}{t_b}\right) = A\exp(BU/t_b) \qquad (3.5)$$

where A and B are temperature dependent material constants, E is the electric field in the oxide, U_{ox} is the potential drop in the oxide and t_b the thickness of the oxide. Since the resistance of the oxide film is usually much higher than the resistance of the electrolyte the potential drop U_{ox} can be approximated as the potential U applied across the cell. As the ions making up the ionic current are also the material from which the oxide grows, the growth rate also follows approximately an exponential relationship.

Even if the anodization is performed in neutral buffer electrolytes, the formation of some additional porous oxide is always to be expected. The possibility of porous oxide growth in pH neutral electrolytes has been ascribed to a decreasing local pH close to the surface during anodization [3, 76-79]. The lower pH increases the possibility of oxide dissolution allowing the formation of pores and continuation of oxide growth. The growth rate is, however, low but if anodizing for longer time significant amount of porous oxide is also formed in these neutral buffer electrolytes [76].

3.2.3.2 Porous-type oxide film

As mentioned above, during anodization porous-type oxide films are formed in acidic electrolytes where the oxide is partly soluble [1, 3]. Typical electrolytes used includes selenic, sulfuric, oxalic, phosphoric, chromic, tartaric, citric and malic acid [1].

The morphology of an ideal porous-type oxide film is shown in Figure 3.8. The oxide contains mutually parallel nanometer-sized pores that extend through almost the entire oxide. The bottom of the pores is closed by a thin hemispherical shaped barrier oxide layer. The pore and the surrounding oxide material forms a hexagonal cell. These cells are positioned in hexagonal close-packed arrangements. Usually, the pore size varies for different pores, and the ordering is far away from the idealized case. However, if using certain electrochemical anodization conditions, the pores can self-organize into larger µm sized domains, where the pores have approximately the same size and are very well ordered, see section 3.2.3.3. The structure of porous oxides are defined by the pore diameter D_p, interpore distance D_{int} and barrier layer thickness t_b, where all parameters are effected by potential, temperature and electrolyte. It has been found that all structural parameters increases and are directly proportional to the anodizing potential, but the proportionality constant varies with temperature and electrolyte as well as the anodization potential regime. The thickness of the barrier layer t_b are related to the potential by a proportionality constant that is lower than 1.4 nm/V, which was the maximum for barrier-type oxides, and have a typical value of 1.1 nm/V [3]. Since the barrier layer thickness is constant and thin, the electric field strength across the layer is high enough to continuously allow ionic transport. This results in an approximately constant growth rate of the porous layer, which final thickness is possible to control

with the anodization time. For corrosion protection properties the porous-type oxide film thickness is commonly grown to 10s of µm, but thicker oxides can be obtained [80].

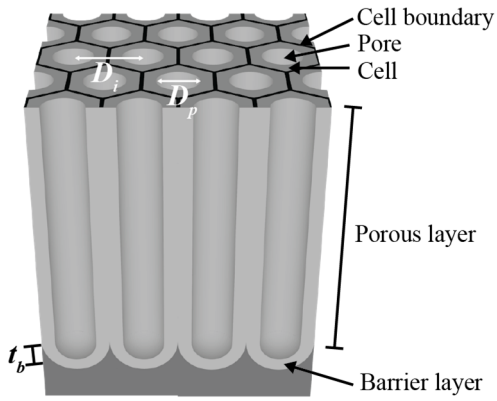

Figure 3.8: Illustration of an ideal porous-type oxide film. t_b: barrier layer thickness; D_i: interpore distance; D_p: pore diameter.

The formation process of porous-type oxides is commonly divided into four regions as illustrated in Figure 3.9, where (a) is a typical current characteristic during anodization at a constant potential and (b) show the different morphologies of the oxide during the anodization. When a potential is applied, a compact barrier anodic oxide film begins to grow across the entire surface (region I). As the oxide thickens the electric field strength decreases, which in turn decreases the ionic current and the growth rate. After a minimum have been reached the current increases again (region II). In this region, the electric field is concentrated on local imperfections (defects, impurities, pits) in the oxide [81]. It has also been proposed that imperfection is formed by local cracking of the barrier layer due to tensile stress in the oxide [1, 82]. Electrolyte then penetrates the cracks or other imperfections where the electric field strength will be higher due to a shorter distance to the Al. The locally increased electric field strength in the cracks polarizes the Al-O bonds, facilitating field-assisted dissolution of the oxide, which leads to the development of the cracks into small disordered incipient pores [39, 82]. As the dissolution thins the barrier layer in the incipient pores also the electric field strength increases, that results in further increase of the ionic current, dissolution and oxide formation rate.

As the electric field strength further increases, some of the incipient pores develop into larger pores by increasing in size and by merging with neighboring incipient pores, while other incipient pores terminate [83, 84]. These larger pores are the pores that are associated with porous-type oxide films. The development towards the larger pores also decreases the pore density, which has been proposed to cause the

local maxima and the decreasing current (region III). Afterwards, the current is approximately stable, but the pores are still gradually rearranging towards a situation where they are ordered in hexagonal domains, and each pore have the same size (region IV). This rearrangement process can, if the correct anodization conditions are used, result in self-ordered NP-AAO (see section 3.2.3.3).

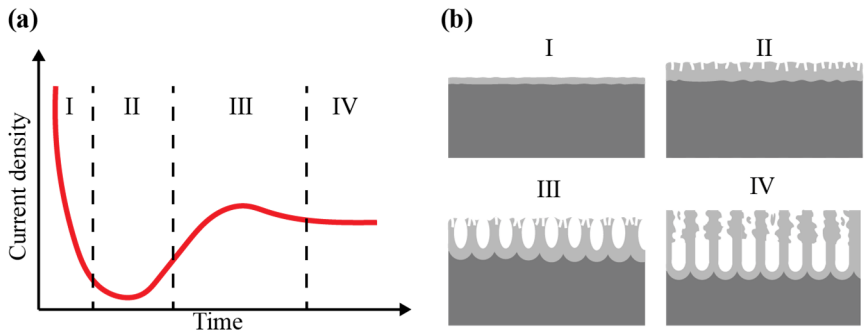

Figure 3.9: Illustration of the formation of porous-type oxide films. (a) Typical current characteristics during porous-type oxide growth at constant anodization potential. (b) Oxide morphology corresponding to the regions (I-IV) marked in the current transient plot (a).

The driving force behind the development of the larger pores and the steady state growth of them is not known and highly debated. For the steady state growth, oxide formation should occur without an increase of the barrier layer thickness below the pores, as this would eventually result in the termination of ionic transport and oxide formation. For a long time, it was believed that oxide formation occurred at both metal/oxide and oxide/electrolyte interfaces and that local field-assisted dissolution of the oxide below the pores was the reason behind the locally maintained barrier layer thickness, pore formation and growth of the larger pores. However, this model was rejected as it does not correctly explain some of the experimental results, especially the amount of Al^{3+} ions in the electrolyte, which is higher than possible if the Al^{3+} ions mainly originate from the dissolution that results in pores [1]. Instead, two other models, have been proposed to explain pore formation, pore growth and self-ordering.

In both these models, oxide formation occurs only at the metal/oxide interface, and the Al^{3+} ions that are migrating towards the electrolyte/oxide interface are directly ejected into the electrolyte without taking part in oxide formation. In the first model, the driving force for pore formation is mechanical stress that induces flow of oxide material [39, 83], from the pore base towards the pore bottom and further to the cell boundary. Compressive stresses generating the flow have been proposed to be caused by electrostriction due to the electric field, and volume expansion due to a larger volume of the oxide formed than the Al consumed [38, 83, 85], where the

stress from both causes are highest below the pore where the electric field strength is highest.

In the second model, the driving force for pore formation is electric-field assisted oxide decomposition at the oxide/electrolyte interface and oxide formation at the metal/oxide interface [86, 87]. The oxide at the pore base is decomposed to Al^{3+} ions that are leaving the oxide together with the other ejected Al^{3+} ions, but the O^{2-} ions are instead driven by the high electric field strength towards the metal/oxide interface where it forms new oxide. The pores are in this model formed by the movements of the metal/oxide and oxide/electrolyte interfaces due to oxide formation and decomposition, respectively, and which rates are determined by the electric field strength that is highest below the pores.

To conclude, both these driving forces have been used in models to explain features occurring during anodization experiments, but the models are still in development [68, 86-88]. For example, the effect of incorporated anions in the oxide has not been accurately accounted for, and the two driving forces have not been combined in one model [89]. For further improvements and to determine the correct driving force for pore formation, experiments are needed to be performed where the oxide morphology is evaluated together with important model parameters such as stress, preferably *in situ* as the oxide is growing. Further discussion of the growth and the models can be found in ref. [1, 69, 89].

3.2.3.3 Ordered nanoporous anodic aluminum oxides (NP-AAO)

In 1995, it was reported that the pores can for certain anodization conditions gradually self-organize such that the pores at the bottom of the produced oxide after several hours or days of anodization are organized in hexagonal μm sized domains [8]. Shortly afterwards, the two-step anodization process was developed, where the pores in the produced oxide have the same size and are ordered through the entire film [9]. Figure 3.10 show illustrations of the oxide morphology during the two-step anodization process [1]. The process begins with a polished Al substrate, either electrochemically and/or mechanically (Figure 3.10 (a)). The Al substrate is then anodized the 1st step using one of the anodization conditions were the pores self-organize. At the beginning of the step, the pores are disordered (Figure 3.10 (b)). However, during the step the pores self-organize and the final produced oxide after hours or longer time of anodization have ordered pores at the bottom but also disordered pores at the top, which are left from the beginning of the anodization (Figure 3.10 (c)). The oxide is then removed by immersing the Al substrate in a solution containing H_3PO_4 and CrO_3, which preferentially dissolves (strip) the oxide without significantly affecting the Al below [90]. The surface after the stripping has approximately hemispherical concaves ordered in the same way as the bottom of the pores (Figure 3.10 (d)). The substrate with ordered concaves is then anodized

the 2nd step using the same conditions as for the 1st step. This time pores initiate and develop in the center of each concave, instead of randomly, such that pores are already ordered in the beginning of the step (Figure 3.10 (e)). This guided pore initiation have been proposed to occur due to a thinner native oxide and as a result a higher electric field strength in the bottom of the concaves [84]. The final produced NP-AAO have ordered pores through the entire porous layer (Figure 3.10 (f)).

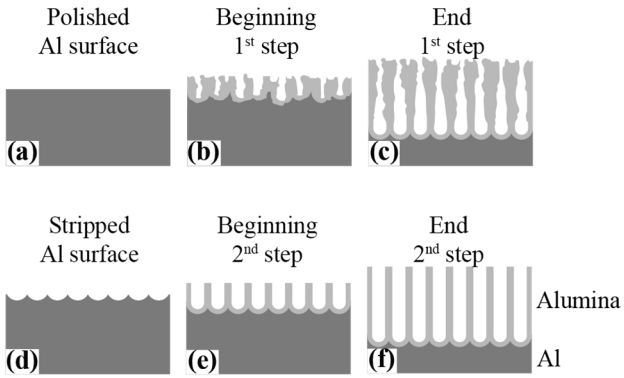

Figure 3.10: Illustration of the steps during the two-step anodization process. (a) Polished surface before the 1st anodization step. (b) Disordered pores formed in the beginning of the 1st anodization step. (c) Produced oxide after the 1st anodization step where the pores are disordered at the top, but ordered at the bottom. (d) Al surface with nanoconcaves left after stripping of the oxide produced in the 1st step. (e) Ordered pores formed in the beginning of the 2nd anodization step. (f) Produced oxide after 2nd anodization step where the pores are ordered through the entire oxide.

The anodization conditions that result in self-ordered NP-AAO is called self-ordering regimes. In the presented thesis self-ordered NP-AAO were studied in chilled (~5 ºC) 0.3 M H_2SO_4 and 0.3 M $C_2H_2O_4$ electrolytes, where the best ordering is obtained at 25 V and 40 V, respectively. These results in NP-AAO with interpore distances of about 60 nm and 100 nm. These conditions are in the mild anodization regime, where the interpore distance increases linearly with potential according to a proportionality constant of 2.5 nm/V [1, 91]. If the anodization is performed outside the anodization regime, the ordering drastically decreases.

In Figure 3.11, three AFM images are shown of NP-AAO surfaces produced using the 2-step anodization process in (a) 0.3 M H_2SO_4 at 25 V, (b) 0.3 M $C_2H_2O_4$ at 40 V and (c) 2 M H_3PO_4 at 150 V. In the case of (a) and (b), the pores are well ordered in hexagonal domains and the size distribution of the pores are small. However, in (c), the ordering is worse and the size distribution is larger. The ordering would have been better if the anodization had been performed at 160 V, which is the potential where the best ordering is obtained in this electrolyte [91].

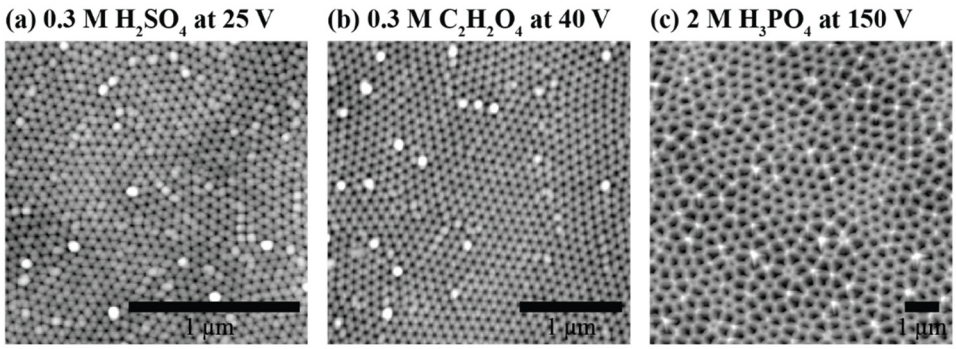

Figure 3.11: AFM images of NP-AAO surfaces produced using the 2-step anodization process in (a) 0.3 M H_2SO_4 at 25 V, (b) 0.3 M $C_2H_2O_4$ at 40 V and (c) 2 M H_3PO_4 at 150 V. Pores are the darker features.

The reason for the self-organization is as with the reason for the pore formation still not known. In the case of the flow model, it has been proposed that small repulsive forces between neighboring pores due to moderate mechanical stresses at the metal/oxide interface at the certain anodization conditions lead to the self-organization [91, 92]. However, based on numerical simulations using the second model where the pore growth is driven by electric-field assisted decomposition and oxide formation, it has been shown that self-ordering can occur without taking into account stresses in the oxide [86, 87].

3.2.3.4 Process for electrochemical deposition into NP-AAO

One of the most promising applications of NP-AAO is for nanotechnology, where the porous material acts as a template or mask for the growth of a large variety of possible nanostructures, see for example [1, 10-13]. The shape and density of the grown structures can be tuned by producing NP-AAO with pores that have the same shape as the desired structures. After the growth, free-standing nanostructures can be obtained by removal of the NP-AAO. Alternatively, the Al substrate can be removed and the bottom of the pores can be opened forming a NP-AAO membrane with the nanostructures inside the pores.

Typical techniques for the nanostructure growth includes atomic layer deposition (ALD), chemical vapor deposition (CVD), physical vapor deposition (PVD) and electrochemical deposition (ECD). Compared to the other mentioned techniques, ECD is inexpensive as fewer process stages are needed and are possible to perform directly in the same setup as the anodization. In the present thesis, only ECD was studied.

ECD has been used for the deposition of metals into porous oxides long before the discovery of the ordered NP-AAO. This process was performed to give the anodized material color, which is also why it is called electrolytic coloring [80]. In the present

thesis, Sn was deposited into the pores of NP-AAO. Deposition of this metal is commonly used industrially to provide anodized Al material with different shades of brown, where the darkest color possible obtained is black.

In the present thesis, Sn was deposited into the pores from a solution including $SnSO_4$, resulting in Sn^{2+} and SO_4^{2-} ions in the solution. An alternating current was used for the deposition. The Sn^{2+} ions are reduced and deposited during the cathodic half cycle of the AC potential, but does not reoxidize in the anodic half of the cycle [93]. This behavior is explained by the rectifying properties of the anodic oxide where the oxide pass current easier in the cathodic direction [3, 94].

The ECD can be performed directly after the anodization if the barrier layer is thin and have low enough resistance to allow electrons through the oxide. However, for the NP-AAO and the process studied in the present investigation, barrier layer thinning processing stages were used to lower the resistance of the barrier layer and enhance the deposition rate. The thinning was done by chemical etching, where also the pores are widened, and by decreasing the anodization potential [95, 96]. The chemical etching, or so-called pore widening was performed by increasing the temperature of the electrolyte after the anodization, which increases the dissolution rate of the oxide and hence widens the pores as well as thins the barrier layer. For the second method, the anodization potential was reduced in steps starting from the potential that was used to produce the NP-AAO. In the beginning of each step, the ratio between oxide formation and dissolution is lower than the previous step resulting in the thinning of the barrier layer [96]. As the layer thins, the oxide formation rate increases. Hence, the thinning proceeds until the formation and dissolution rates are equal and a certain thickness that corresponds to the potential has been reached. The final thickness of the barrier layer after all potential steps corresponds to the lowest potential applied. The entire process is illustrated in Figure 3.12 (a), where (I) is the NP-AAO as obtained after the two-step anodization process, (II) is after the chemical etching, (III) is after decreasing the anodization potential and (IV) is after deposition of Sn into the pores. Figure 3.12 (b) and (c) is photos of Al substrates with NP-AAO before and after deposition, respectively. Figure 3.12 (d) is an SEM image of a trench that has been made in a NP-AAO after Sn deposition, where the oxide is seen from the side with the Sn as the brighter rods in the pores.

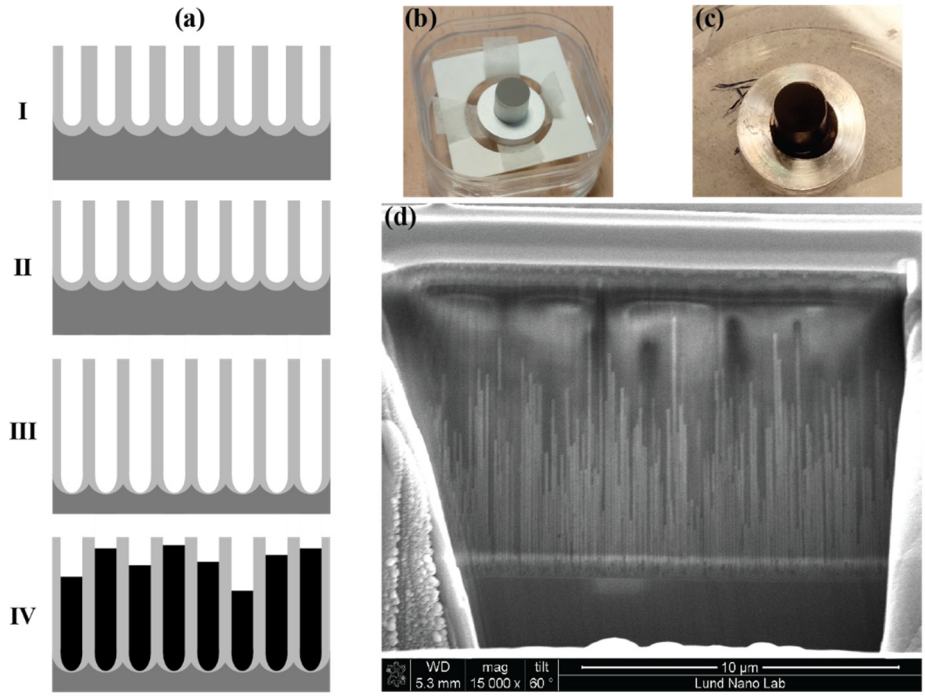

Figure 3.12: (a) illustrates the different processing steps (I-IV) performed for deposition of Sn in the present thesis, where (I) is as obtained after the 2-step anodization process, (II) is after chemical etching, (III) is after decreasing anodization potential and (IV) is after deposition of Sn. (b) and (c) are photos of Al substrates with NP-AAO before and after Sn deposition, respectively. (d) SEM image of a trench that has been made in a NP-AAO after Sn deposition, where the oxide is seen from the side, and the Sn is the brighter rods in the pores.

3.2.4 Effect of alloying elements on native and anodic oxides

In the description above, native and anodic oxides have been described as more homogeneous films that have similar thickness across the whole surface. This description is approximately valid for pure Al substrates, but less valid for AA, where the alloying elements in the alloy metal and as intermetallic particles can alter the oxide film. For the native oxide, the intermetallic particles at the surface can have a different susceptibility towards oxidation resulting in thicker or thinner oxide film regions. The alloying elements or the intermetallic particles can also be incorporated into the formed oxide film. These can act as doping, which could allow the oxide to grow thicker.

During anodization, the alloying elements also influence the anodization process as well as the formed anodic oxide [4]. Two layered oxide films can be formed where

the layer consists of more or less of alloying element oxide. Certain alloying elements can result in the formation of oxygen bubbles in the oxide. These bubbles can lead to mechanical damage, roughening and obstruction of ionic migration, which can result in thinner barrier layer thicknesses. Alloying elements that when forming oxides expands less than when aluminum forms oxide, can result in voids at the metal/oxide interface.

The general conclusion is that anodic oxide films on aluminum alloys can be significantly different from that on pure aluminum and hence have other properties. This has, as already mentioned, a high impact on the corrosion resistance properties of the material. It also affects the porous morphology, where for example the self-ordering of NP-AAO grown on aluminum alloys substrates are worse than on pure aluminum substrates [97]. It is therefore important to study the anodization of AA, to be able to develop altered anodization procedures for the alloys where the effect of the alloying elements is taken into account.

4 Experimental methods and setups

Several experimental techniques has been employed for the studies in the present thesis and include various scattering, spectroscopy, electrochemical and microscopy techniques. The chapter begins with methods based on X-rays (section 4.1) where first the scattering techniques and later the spectroscopy methods are introduced. Afterwards, the electrochemical methods (section 4.2) are described, where the focus is on electrochemical impedance spectroscopy (EIS). This is followed by the description of Atomic Force Microscopy (AFM) and Scanning Electron Microscopy (SEM) (section 4.3). Finally, the setups used for the *in situ* studies are described (section 4.4).

4.1 X-ray and synchrotron radiation

In 1895, X-rays were discovered by W. C. Röntgen. Later, M. von Laue, as well as W. H. Bragg and W.L Bragg, developed the X-ray diffraction (XRD) method, where X-rays are used to determine crystal structures and atomic positions. All four were awarded the Nobel prize for their work [98].

X-rays are often produced using a rotating anode generator where electrons from a glowing filament are accelerated towards a water-cooled spinning metal anode [99]. The X-ray spectra generated from these sources are composed of a less intense continuous part, Bremsstrahlung, due to the deceleration of the electrons and more intense sharp lines as the incoming electrons also removes atomic electrons from the inner shells with subsequent X-rays produced as outer shell electrons fills the inner vacancies. These sources have limitations, the intensity is limited by the cooling efficiency of the metal anode, and the radiation is not continuously tunable.

On the other hand, X-rays produced by synchrotrons have much higher intensity, the energy can be tuned over a larger range, and the X-ray beam is narrow. The synchrotron radiation is produced by accelerating charged particles, usually electrons, to relativistic speeds and by forcing them to turn in magnetic fields, in so-called bending magnets, wigglers and undulators. The brilliance is a single quantity used to compare different X-ray sources, where the intensity, the divergence of the beam, the size of the source, and spectral distribution are parameters that are

considered. The brilliance from third-generation synchrotrons, i.e. where all experiments in the present thesis took place, is approximately 10 orders of magnitude higher than from the sharp lines of rotating anodes. It is, therefore, possible with synchrotron radiation to perform intensity demanding experiments that would have been impossible before, such as *in situ* measurements through for example liquids, where higher energy and higher intensity is needed.

In the experiments in the present thesis, we have used X-rays with both lower (>1500 eV) and higher energy (10 – 29 keV). The lower energies are suitable for surface sensitive and thin film XPS studies due to the short mean free path of the produced photoelectrons. However, the short mean free path of the electrons makes *in situ* measurements in an electrolyte very difficult. Instead, by using higher x-ray energies, and detect scattered x-rays with the same energy, we can circumvent the problem with short penetration depth in the environment. In this way, we can penetrate the cell walls as well as the electrolyte to study anodic oxides in an electrochemical cell by scattering techniques.

4.1.1 X-ray scattering geometries

With X-ray scattering techniques structures with varying sizes are probed by studying the reciprocal space, i.e. the intensity of the sample scattered X-rays. In the present thesis, the X-ray scattering techniques X-ray reflectivity (XRR) and grazing-incidence transmission small-angle X-ray scattering (GTSAXS) were used to probe the morphology of native and anodic aluminum oxides. Figure 4.1 illustrates the geometries of these methods together with X-ray diffraction (XRD) and grazing-incidence small-angle X-ray scattering (GISAXS). For all methods, the incoming X-ray beam of wavevector $\boldsymbol{k}_i$ (black) makes an incidence angle α_i with respect to the surface of the substrate. Depending on the scale of the structures, the scattered X-ray beams of wavevector $\boldsymbol{k}_f$ can be found at different angles 2θ with respect to the direct beam position in the absence of the sample (black). The angle 2θ is also equivalent to the angle components α_f and $2\theta_f$ with respect to the surface plane and the in-plane component of the direct beam, respectively.

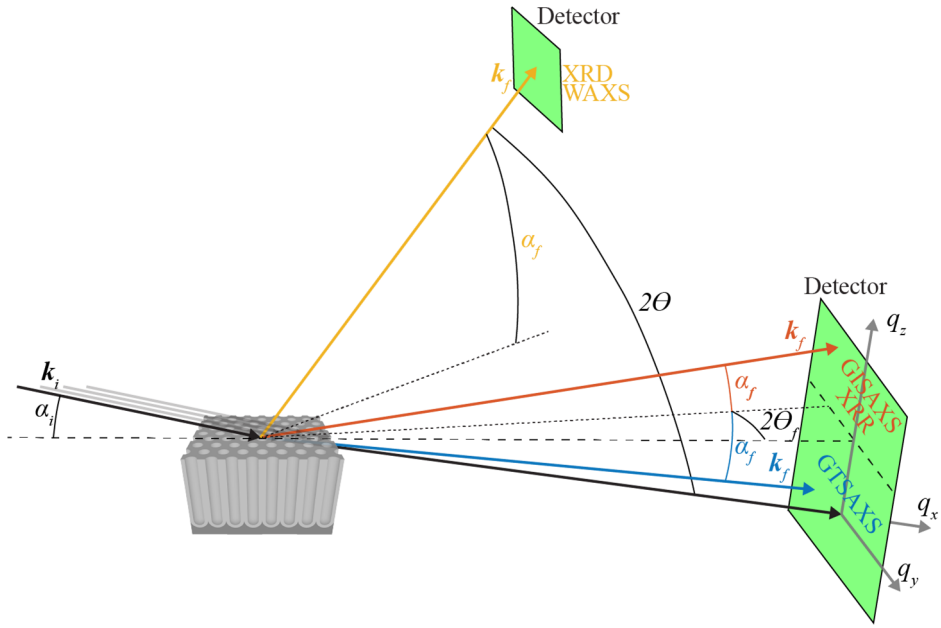

Figure 4.1: Illustration of X-ray scattering geometries. An X-ray beam with wavevector $\boldsymbol{k}_i$ (black) incidence with an angle α_i towards the surface of a NP-AAO substrate. Scattered beams (yellow, red, blue) with wavevector $\boldsymbol{k}_f$ makes an angle 2θ with $\boldsymbol{k}_i$ or, equivalently, the angles α_f and $2\theta_f$ with the surface and the in-plane component of the direct beam (black), respectively. The angles is also related to the wavevector transfer coordinates q_x, q_y and q_z. The wider angle regime is studied in for example XRD and WAXS, where the scattered intensity is commonly measured by scanning with a 2 dimensional detector. The smaller angle regime is instead studied in for example XRR and SAXS, where a stationary detector is commonly used. The SAXS region is divided into GISAXS and GTSAXS, where the reflected or transmitted scattering is studied, respectively. Partly adapted from [100].

The difference between wavevectors $\boldsymbol{k}_i$ and $\boldsymbol{k}_f$ is the wavevector momentum transfer $\boldsymbol{q} = \boldsymbol{k}_f - \boldsymbol{k}_i$. The wavevector momentum transfer is also related to the wavevector transfer coordinates (q_x, q_y, q_z), which are calculated from the angles α_f and $2\theta_f$ according to:

$$\begin{aligned} q_x &= k_0\left[\cos(2\theta_f)\cos(\alpha_f) - \cos(\alpha_i)\right] \\ q_y &= k_0\left[\sin(2\theta_f)\cos(\alpha_f)\right] \\ q_z &= k_0\left[\sin(\alpha_f) + \sin(\alpha_i)\right] \end{aligned} \tag{4.1}$$

where $k_0 = 2\pi/\lambda = k_i = k_f$ is the wavevector modulus that are equal to k_i and k_f as the X-rays are elastically scattered. λ is the wavelength of the X-rays and is related to the energy E as $\lambda(\text{Å}) = 12400/E(eV)$.

Typical methods in the wider angle regime are wide-angle X-rays scattering (WAXS) and XRD, where atomic length scales in a crystal structure can be studied. For these methods, a movable two-dimensional detector is commonly used such that a large range of the reciprocal space is possible to probe by scanning with the detector. It is also possible to use a stationary detector for these methods, by placing the detector very close to the sample or by the use of high energy X-rays [44].

In the smaller angle regime, SAXS and XRR are typically used methods, where the studied length scales are in the nm range such as pores in NP-AAO. For these methods, a stationary detector is used which covers a large part of the relatively small reciprocal space since the structures are relatively large. The regions in reciprocal space probed by GISAXS and GTSAXS is also illustrated on the detector in Figure 4.1. In GISAXS, the reflected scattering above the surface horizon is used. In GTSAXS, the transmitted scattering below the surface horizon is instead used.

In the following sections are XRD, GTSAXS and XRR, as well as the grazing incidence geometry described. XRD was not directly used in the present thesis, but is described here since it is a traditional method were X-ray scattering is used and since the theory of diffraction from crystals is applicable for other system with periodic lattices such as NP-AAO.

4.1.2 X-ray diffraction (XRD)

Diffraction is used to study periodic structures, and reveal properties such as unit cell dimensions, the presence of different phases and the atomic positions in crystals. It makes use of two properties of waves; that objects scatter the waves in all directions and the constructive or destructive interference occurring when the waves meet and interact, in or out of phase, respectively. By measuring the intensity variations due to the interference in three dimensions, it is possible to achieve a map of the reciprocal lattice corresponding to the real lattice of the crystal. It is, therefore, possible to retrieve the real crystal structure from the diffraction pattern.

By using X-rays with wavelengths of the same order or shorter than the lattice constant of crystals it is possible to study the atomic structure of crystalline materials. In the crystal, it is the spatial distribution of the electrons in the lattice cell that is responsible for the scattering of the X-rays, and it can in a simplified way be said that the atoms act as scatterers. Since the X-rays only interact weakly with the atoms it is possible to describe the scattering processes by a kinematical scattering theory, i.e. the scattered waves are only scattered elastically and once in the crystal. The theory of X-ray diffraction from crystals is described in for example ref. [53].

W.L. Bragg explained the X-ray diffraction from crystals assuming that the atoms in the crystal constitute equally spaced parallel planes, where a small fraction of an incident X-ray beam is reflected at each plane, see Figure 4.2. The reflected X-rays will interfere constructively into an intense diffracted beam only when the path difference is equal to a multiple of the wavelength of the X-rays. This is summarized in the Bragg equation

$$2d \sin\theta = n\lambda \tag{4.2}$$

where d is the distance between adjacent parallel planes, θ is the angle between the planes and the incoming beam, n is an integer and λ is the X-ray wavelength. As there are several possible parallel planes in a crystal, diffracted beams can be found for several angels θ where each diffracted beam corresponds to a specific distance between adjacent planes.

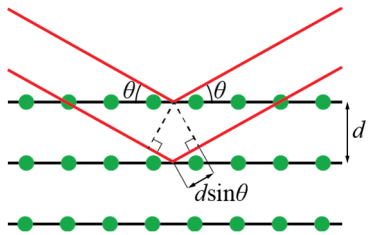

Figure 4.2: Illustration describing the Bragg equation. A small fraction of an incident X-ray beam (red) is reflected at each parallel plane of atoms (green). For certain angles θ and wavelenghts the reflected X-rays will interfere constructively into an intense diffracted beam.

Another way of describing X-ray diffraction is shown in Figure 4.3 for two atoms separated by a vector $\boldsymbol{R}$. The incoming X-ray beam, described by the wavevector $\boldsymbol{k}_i$, is scattered by the two atoms into another direction, and then described by the wavevector $\boldsymbol{k}_f$. As only elastically scattered waves are considered, the magnitude for both wavevectors are equal and related to the wavelength λ according to

$$k = \boldsymbol{k}_i = \boldsymbol{k}_f = \frac{2\pi}{\lambda} \tag{4.3}$$

Constructive interference between the outgoing waves from the two atoms occurs when the path difference PD is equal to an integer number of wavelengths $n\lambda$, i.e. when the waves are in phase. This can also be described using the wavevectors and the vector $\boldsymbol{R}$ between the atoms

$$\frac{\boldsymbol{R}\cdot\boldsymbol{k}_f}{k} - \frac{\boldsymbol{R}\cdot\boldsymbol{k}_i}{k} = \frac{\mathbf{R}\cdot\boldsymbol{\Delta k}}{k} = s + s' = PD \;=\; n\lambda = n\frac{2\pi}{k} \tag{4.4}$$

where $\boldsymbol{\Delta k} = \boldsymbol{k}_f - \boldsymbol{k}_i$ is the wavevector momentum transfer at diffracting conditions. From this, it is deduced that constructive interference occurs when

$$\mathbf{R} \cdot \boldsymbol{\Delta k} = 2\pi n \tag{4.5}$$

which is known as the Laue formalism of diffraction.

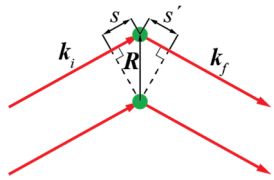

Figure 4.3: Illustration of an X-ray beam (red) scattered by two atoms. The scattered beams interfere constructively if the path difference ($s + s'$) is equal to a multiple of the wavelenght.

The crystal is a 3-dimensional object, therefore the real lattice is described by the vector

$$\boldsymbol{R} = m_1\boldsymbol{a_1} + m_2\boldsymbol{a_2} + m_3\boldsymbol{a_3} \tag{4.6}$$

where m_1,m_2 and m_3 are integers. To describe all the possible $\boldsymbol{\Delta k}$ resulting from a crystal, the reciprocal lattice is used. The reciprocal lattice is related to the real lattice by a Fourier transform and described by

$$\boldsymbol{G} = h\boldsymbol{b_1} + k\boldsymbol{b_2} + l\boldsymbol{b_3} \tag{4.7}$$

where h, k and l are the Miller indices. The real and reciprocal basis vectors are related as

$$\boldsymbol{b_1} = 2\pi\frac{\boldsymbol{a_2}\times\boldsymbol{a_3}}{\boldsymbol{a_1}\cdot\boldsymbol{a_2}\times\boldsymbol{a_3}};\ \boldsymbol{b_2} = 2\pi\frac{\boldsymbol{a_3}\times\boldsymbol{a_1}}{\boldsymbol{a_1}\cdot\boldsymbol{a_2}\times\boldsymbol{a_3}};\boldsymbol{b_3} = 2\pi\frac{\boldsymbol{a_1}\times\boldsymbol{a_2}}{\boldsymbol{a_1}\cdot\boldsymbol{a_2}\times\boldsymbol{a_3}} \tag{4.8}$$

The basis vectors follow the same argument for constructive interference as in equation (4.5), and it is possible to show that intense reflections are achieved when $\boldsymbol{\Delta k} = \boldsymbol{G}$ and negligibly small otherwise. With this in mind, it is obvious that by performing a Fourier transform of the measured diffraction pattern, i.e. reciprocal lattice, the real lattice of the crystal can be obtained.

4.1.3 Grazing incidence geometry

In general, as X-rays only interact weakly with matter, they penetrate deep into the bulk of materials. Hence, the contribution from the surface in the total signal from conventional bulk diffraction patterns is low. However, due to the refractive properties of X-rays compared to for example optical light, it is possible to increase the signal from the near-surface region by using small incidence angles, i.e. grazing incidence. An extensive description is found in, for example, ref. [99, 101].

For X-rays, the refractive index of a medium is given by

$$n = 1 - \delta - i\beta \tag{4.9}$$

where the dispersion coefficient δ is related to the scattering and the absorption coefficient β is related to the absorption properties of the material. Both are small, i.e. δ is of the order of 10^{-6} and β are usually one or two order smaller, and hence, the refractive index is slightly smaller than unity. The fact that the refractive index is less than unity results in what is called total external reflection for angles lower than a critical angle α_c, as the X-ray will approximately be totally reflected. The critical angle α_c can be obtained using Snell's law $\cos\alpha_c = n\cos\alpha_i'$ and approximated, since the angle is small, by an expansion of the cosine:

$$\alpha_c \approx \sqrt{2\delta} \tag{4.10}$$

To describe the penetration depth and the amplitudes of the refracted and reflected X-ray wave, the situation in Figure 4.4 is commonly used. In the figure, a linearly polarized X-ray wave with amplitude $\boldsymbol{E}_i$ and wavevector $\boldsymbol{k}_i$ is incident with an angle α_i on to a surface, i.e. a sharp interface between vacuum and a material with refractive index n, where the wave is divided into a refracted ($\boldsymbol{E}_i'$, $\boldsymbol{k}_i'$) and a reflected ($\boldsymbol{E}_r$, $\boldsymbol{k}_r$) part. Using Snell's law the relation between the angles is achieved as follows

$$\cos\alpha_i' = (\cos\alpha_i)/n \tag{4.11}$$

which by an expansion of the cosine and by neglecting absorption gives

$$\alpha_i'^2 \approx \alpha_i^2 - \alpha_c^2 \tag{4.12}$$

From the equation, it can be seen that α_i' is imaginary, if neglecting absorption, for $\alpha_i < \alpha_c$. From this it follows that the vertical component of the wavevector $\boldsymbol{k}_i'$, $k_{i,z}' = knsin(\alpha_i')$, is also almost only imaginary and as a consequence the refracted wave is exponentially damped and the wave travels only as an evanescent wave almost parallel to the surface with a penetration depth of a few nm.

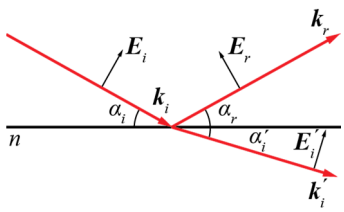

Figure 4.4: A linearly polarized plane wave incident on a sharp interface between vacuum and a material with refractive index n. Adapted form [101].

Including also absorption, the 1/e penetration depth Λ is given by [101]

$$\Lambda^{-1} = \sqrt{2}k\left(\sqrt{(\alpha_i^2 - \alpha_c^2)^2 + 4\beta^2} + \alpha_c^2 - \alpha_i^2\right)^{1/2} \tag{4.13}$$

Figure 4.5 shows the 1/e depth of penetration for X-rays with an energy of 24 keV incident on aluminum and alumina calculated using equation (4.13) and using data from ref. [102, 103]. The penetration depth is below 10 nm for incident angles smaller than the critical angle of 0.07° and 0.09° for aluminum and alumina, respectively. This means that it is beneficial to use smaller incidence angles for studies of the near-surface region, but as will be discussed below also complicates the analysis of the measured scattering.

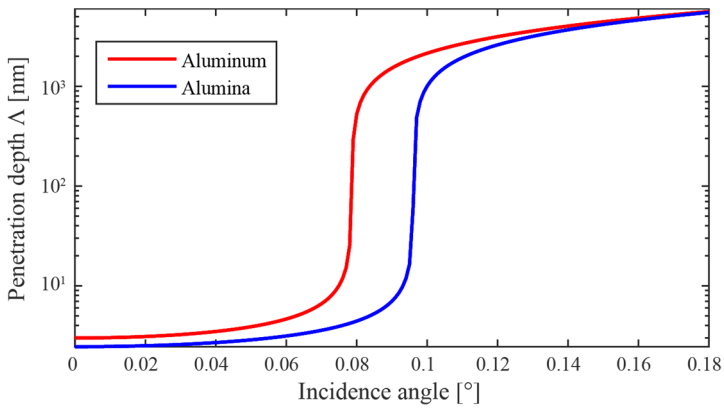

Figure 4.5: The 1/e depth of penetration of 24 keV X-rays in aluminum and alumina. The penetration depth is below 10 nm for incident angles below the critical angle and much higher at angles above the critical angle.

4.1.4 Grazing-incidence transmission small angle X-ray scattering (GTSAXS)

Using small angle X-ray scattering (SAXS), larger structures in the range from about 1 nm to several 100 nm can be studied and are therefore suitable for studies of for example NP-AAO. Using SAXS, properties such as the shape, size and structure can be obtained, provided that the nano-objects are positioned periodically. As a large volume can be probed by the incoming X-rays, better statistics is achieved compared to microscopy techniques as the latter techniques are limited to smaller areas. Another advantage of SAXS is that also properties from the bulk below the surface can be obtained. Such bulk properties are difficult or even impossible to

obtain from microscopy, without sample preparations such as cleaving or thinning the sample. SAXS is also suitable for *in situ* studies by using an incoming X-ray beam with high enough energy and intensity.

A common variant to study nano-objects on or close to surfaces is grazing-incidence small-angle X-ray scattering (GISAXS) [104]. With this technique, an incidence angle close to the critical angle is used to minimize the effect of background scattering from the bulk and increase the scattering from the studied objects close to the surface due to total external reflection [100]. However, a drawback with using a low incidence angle is that the measured pattern is distorted significantly by refractive and multiple reflective effects, which in turn complicates the analysis of the GISAXS pattern [105].

More recently, another variant of SAXS was introduced, namely grazing-incidence transmission small-angle X-ray scattering (GTSAXS) [105]. With this technique a higher grazing incidence angle α_i is used and the transmitted beam through the side of the sample is analyzed instead. Figure 4.6 (a) illustrates the GISAXS and GTSAXS geometries. An incident X-ray beam impinges with an angle a_i towards the surface of the substrate and the scattered beam is measured by a two dimensional detector. The sample horizon (dashed line) divides the measured pattern into the GISAXS and GTSAXS regimes. The illustration also shows that the transmitted beam is slightly refracted and moves the GTSAXS pattern from $q_z = 0$ (dotted line) towards the surface. However, this effect is small for higher incidence angles and was in the present thesis ignored.

Figure 4.6 (b) show detector images recorded at incidence angle $\alpha_i = 0.1°$, $\alpha_i = 0.2°$, and $\alpha_i = 0.5°$ of an NP-AAO after anodization in 0.3 M H_2SO_4 at 25 V. The surface horizon (dashed line) divides the detector images into the GISAXS (above) and GTSAXS (below) regimes. At $\alpha_i = 0.1°$, the reflected contribution (red arrow) is close to the transmitted contribution (yellow arrow). At $\alpha_i = 0.2°$, the contributions are more separated, where the reflected contribution is above the detector. The transmitted contribution is also more intense. At $\alpha_i = 0.5°$, the contributions are further separated and the transmitted contribution is less refracted and approximately found at $q_z = 0$. This undistorted and clean transmitted pattern at the higher grazing-incidence angles is well described by the simple born approximation, where only scattering of the incoming beam is considered without the need to take into account contributions due to reflection, which is the case for GISAXS [105]. Hence, the analysis of GTSAXS patterns is simpler than the analysis of GISAXS patterns. In addition, the incidence angle is still small enough to probe the structure normal to the surface, which is difficult using transmission small-angle X-ray scattering (TSAXS), where much higher incidence angles are used and the scattered beam exits through the bottom of the sample.

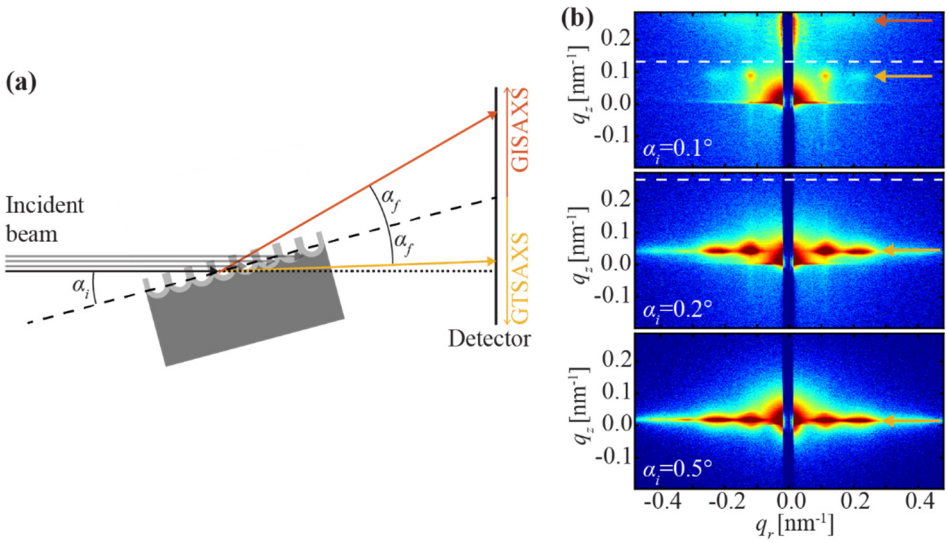

Figure 4.6: (a) Illustration of the GTSAXS and GISAXS geometry. An incident X-ray beam impinges with a grazing incidence angle α_i towards the substrate surface and the scattered beam is measured by a detector. The surface horizon is indicated by the dashed line and divides the measured pattern into the GISAXS and the GTSAXS regimes. The dotted line indicates the position of a direct non-refracted beam and shows that the transmitted beam (yellow) are refracted towards the surface. (b) Detector images recorded at incidence angle $\alpha_i = 0.1°$, $\alpha_i = 0.2°$, and $\alpha_i = 0.5°$ of an NP-AAO after anodization in 0.3 M H_2SO_4 at 25 V. Red and yellow arrows indicates the position of the reflected and the transmitted contributions. The dashed line indicates the surface horizon.

In the present thesis, the measured patterns were analyzed by first extracting profiles along the $q_r = (q_x^2 + q_y^2)^{1/2}$ and the q_z directions from the images. The profiles were then fitted to obtain the interpore distance, the domain size of ordered pores and the thickness of the NP-AAO. Figure 4.7 illustrates the analysis procedure in the q_r direction from which the domain size and the interpore distance were determined. Figure 4.7 (a) is part of the detector images recorded at 0 s (I), 200 s (II) and 6000 s (III) of the 1st anodization step in 0.3 M H_2SO_4 at 25 V for an Al(110) substrate. The white rectangles shows the area from which the profiles were extracted. These profiles subtracted with the profile at 0 s as a background are shown to the left in Figure 4.7 (b).

The extracted profiles correspond to the average of the entire NP-AAO that have been grown. As the oxide formation and the ordering of the pores mainly occur at the metal/oxide interface, it would be preferable to analyze the contribution in the profile that corresponds to the bottom part of the oxide. This was achieved by analyzing the difference between profiles, as the difference is approximately only due the newly formed layer at metal/oxide interface during the time between the profiles. The way the difference was determined is described in paper V-VI. The obtained difference between profiles is shown to the right in Figure 4.7 (b).

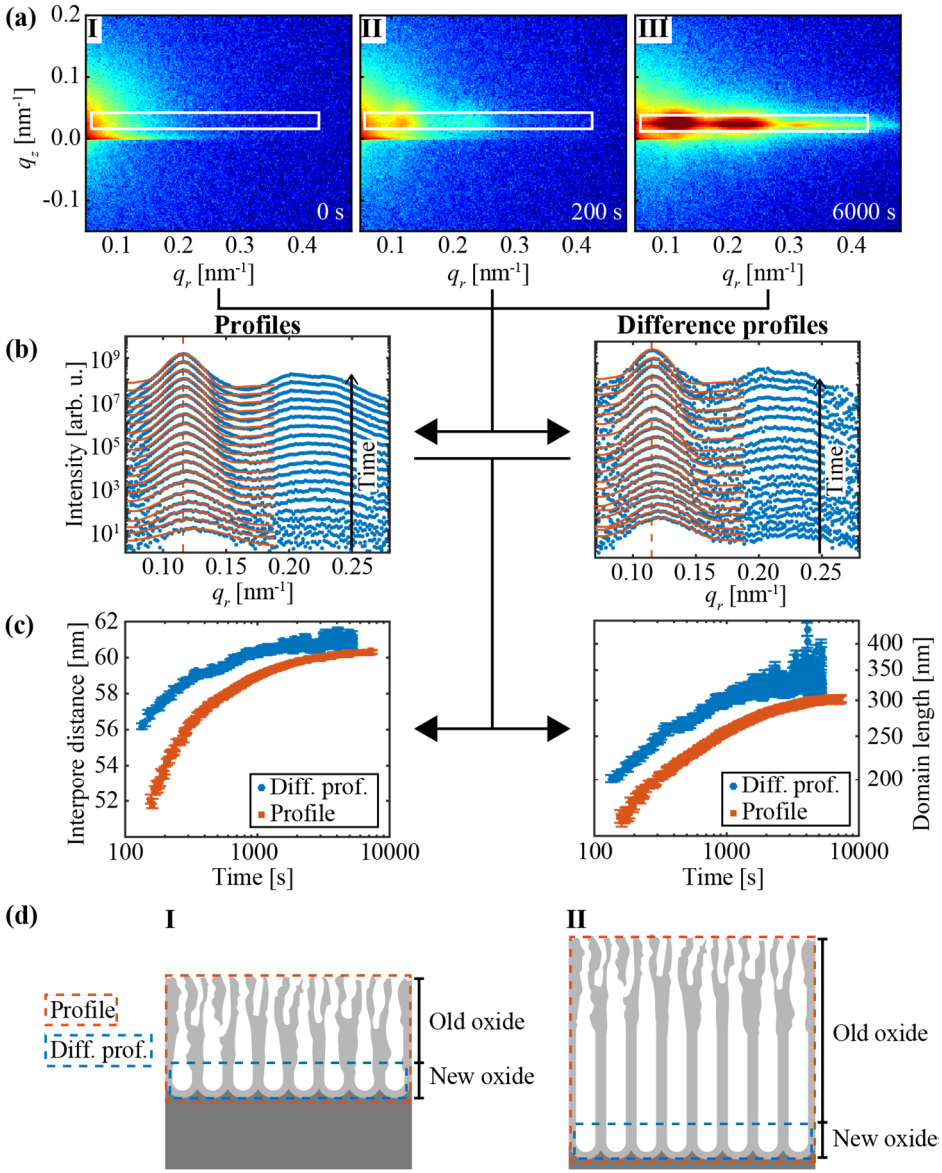

Figure 4.7: Analysis procedure of the profiles in the q_r direction. (a) Detector images recorded after (I) 0 s, (II) 200 s and (III) 6000 s of the 1st anodization step in 0.3 M H_2SO_4 at 25 V for an Al(110) substrate. White rectangle is the area from which the profiles were extracted. (b) Left: Profiles (blue dots) extracted from the images and subtracted with the profile at 0 s. Right: Differences between the profiles. Red lines is fits to the profiles and difference profiles. (c) Interpore distance and domain length obtained from the fits of the profiles and the difference profiles. (d) Illustrations to explain the difference between the results obtained from fits of the profiles and difference profiles. The NP-AAO in the (I) beginning and (II) after longer time of anodization.

The profile intensity $I(q_r)$ is described by

$$I(q_r) = A|F(q_r)|^2 S(q_r) \quad (4.14)$$

where A is a scale factor, F is the form factor and S is the structure factor. The form factor F is the Fourier transform of the nanostructure shape, and the structure factor S is the Fourier transform of the radial distribution function of the nano-objects position [100]. In the case of ordered structures where the nano-objects are positioned according to a lattice, the structure factor will consist of well-defined high intensity peaks similar to XRD data from single crystals, see section (4.1.2). With decreasing ordering, the intensity of the peaks decreases. For fully disordered systems the structure factor tends to unity and the measured intensity is determined by the form factor alone [100].

The pores in self-organized NP-AAO are rather ordered. Hence, to fit the profiles both the structure and form factor was taken into account using a combination of the models in refs. [106, 107] and as further described in paper V. As the pores are positioned in domains according to a 2-dimensional hexagonal lattice, the structure factor peaks can be found at

$$q_{hk} = \frac{4\pi\sqrt{h^2+hk+k^2}}{\sqrt{3}a}, \quad (4.15)$$

where a is the lattice constant, i.e. interpore distance, and h,k are the Miller inidices. The shape of the peaks were approximated with a Gaussian line profile. The pores were approximated using the form factor of a hollow-shell cylinders sitting in an alumina matrix, to take into account the duplex nature of the pore walls due to anion incorporation.

Due to poor statistics of the data and probably that the model does not take into account all structural parameters of the NP-AAO, such as the hemispherical pore bottom, the correlation between parameters were high. This resulted in the obtained fitted parameters shifting in a non-continuous unrealistic manner. To account for this, the form factor parameters were fixed, and the fitted range was limited. The obtained fits (red lines) are shown in Figure 4.7 (b) for the profiles and the difference profiles. The interpore distance was calculated from the positions of the structure factor peaks, and the domain size D were calculated from structure factor peak width Δq_r using the Scherrer equation: $D = 2\pi/\Delta q_r$.

The 1st order reflection peak in both the profiles and the difference profiles shift towards smaller q_r values and decreases in width with anodization time, which corresponds to an increasing interpore distance and domain length, respectively. This is also seen in the obtained values shown in Figure 4.7 (c) for the fits of the profiles (red) and difference profiles (blue).

The different values obtained from the fits of the profiles and difference profiles are explained by the illustrations in Figure 4.7 (d). In the beginning (I), the interpore distance changes much, which means that there is a large difference between the old and newly formed oxide. Hence, there will also be a large difference between the profiles that correspond to the mean of the entire NP-AAO and difference profiles that only corresponds to the newly formed oxide. As the anodization proceeds, the interpore distance stabilizes, which means that the old oxide will include more oxide that has similar interpore distance as the newly formed oxide. Hence, after longer time of anodization (II), the average structure of the entire oxide will be more similar to the newly formed oxide layer. The difference between the obtained values from the fits of the profiles and the difference profiles will, therefore, decrease with anodization time. Most importantly, this shows that a better estimate of the ongoing evolution of the pores is obtained from the difference profiles.

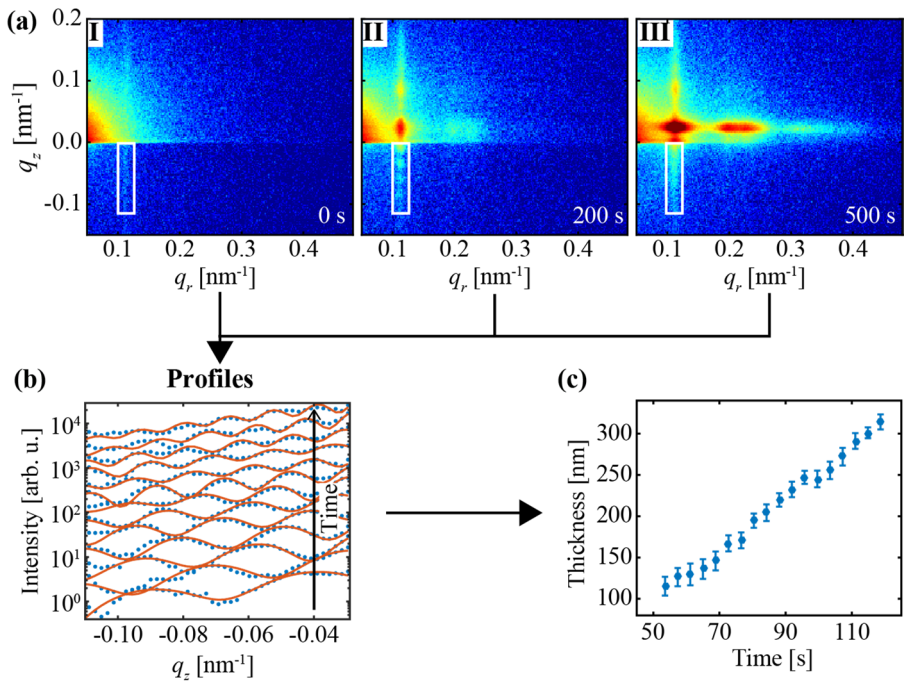

Figure 4.8: Illustration of the analysis procedure along the q_z direction. (a) Detector images recorded after (I) 0 s, (II) 200 s and (III) 500 s of the 2nd anodization step in 0.3 M H_2SO_4 at 25 V for an Al(110) substrate. White rectangle illustrates the area from which profiles were extracted. (b) Profiles (blue dots) as extracted from the images. Red line is fits of the profiles. (c) Thicknesses obtained from the fits in figure (b).

The thickness of the growing oxide could be determined by analysis of the profiles in the q_z direction as illustrated in Figure 4.8. Figure 4.8 (a) shows three detector images recorded at 0 s (I), 200 s (II) and 500 s (III) from the 2nd anodization step in 0.3 M H_2SO_4 at 25 V for an Al(110) substrate. The white rectangles shows the area from which the profiles shown in Figure 4.8 (b) were extracted. The profiles oscillates with q_z. The period of these oscillations is related to the height of the pores or the thickness of the oxide. The thickness t was determined from the distance between the adjacent peaks or equally the period of oscillation Δq_z according to: $t = 2\pi/\Delta q_z$. This is valid for when the top and bottom is flat, which is approximately true for the porous film of the NP-AAO.

4.1.5 X-ray reflectivity (XRR)

X-ray reflectivity (XRR) is a powerful method, which has been used for almost one century to study the electron density profile of layered structures. Quantitative information such as the thickness, roughness and density of layers can be achieved in a nondestructive manner of materials. The method is not limited to crystalline materials, such as in XRD, and can be employed on amorphous as well as on liquid materials.

Compared to other non-destructive methods common for anodic oxide thickness determination, such as EIS, the accuracy is found to be higher for XRR as fewer number of assumptions are used. However, to perform XRR, the surface needs to be very smooth. Literature describing the XRR technique can be found in for example [99, 108-111].

In the present thesis, specular XRR was used, where a measurement is performed by measuring the reflected intensity as a function of the incidence angle of the incoming X-rays on the sample surface. The technique, as well as a simulated result from a single layer thin film, is illustrated in Figure 4.9 (a) and (b), respectively. In (b), it is seen that for low angles, all the intensity of the incoming beam is reflected. At higher angles than the critical, the intensity drops quickly, as $1/q^4$ and superimposed onto the quick drop typically oscillations are observed, i.e. Kiessing fringes. These originates from the interference of X-rays that have been reflected from the different interfaces in the sample. Hence, from the periodicity of the oscillations the thickness of the film can be approximated, as

$$d \approx 2\pi/\Delta q_z \tag{4.16}$$

where Δq_z is the distance in reciprocal space between two maxima.

To determine the thickness more accurately and to achieve more information regarding more complex multilayer systems, there is a need for modeling and fitting the reflectivity curve, which is described in detail in for example [99, 111]. For the

fitting, the recursive Parrat algorithm is used [112]. The algorithm begins with calculating the reflectivity from the bottom layer. This is then used for calculating the reflectivity from the next layer in the stack of layers. Recursively, the reflectivity from all the layers can be calculated and finally also the total reflectivity from the environment-surface interface is obtained. To accurately model a real multilayer system also the roughness of the interfaces needs to be considered. The Névot-Crocet formalism is the most used roughness model, where the electron density of the rough interface is modeled with an error function type profile that results in damping of the reflectivity from the interface [113].

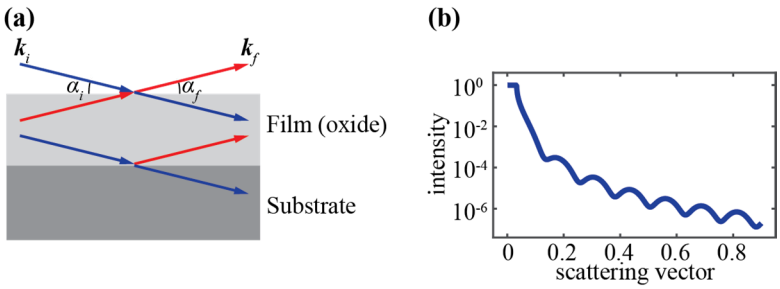

Figure 4.9: (a) Illustration of X-ray reflectivity from a thin film on a substrate. (b) A simulated reflectivity curve. At each interface the incoming beam $\boldsymbol{k_i}$ is transmitted (blue) or reflected (red). The total intensity of the outgoing beam $\boldsymbol{k_f}$ is a superposition of reflections from all interfaces. In the reflectivity curve the charateristic oscillations, Keissing fringes, are shown. From the distance between the fringes it is possible to estimate the thickness. Adapted from [114].

4.1.6 X-ray fluorescence (XRF)

X-ray fluorescence (XRF) is a non-destructive and powerful method for element analysis in solids or liquids and can be used in both gas and liquid environments [115]. It is also suitable for *in situ* analysis of the composition of the solution and sample in an electrochemical cell if the energy of the fluorescence is high enough to penetrate the solution. The method is based on an incoming X-ray beam that excites the atoms in the material such that electrons are ejected, and vacancies are created in the inner shells of the atoms. When electrons from higher shells then drop down to fill the vacancies in the lower shells, photons are emitted, such as X-rays. The energy of the emitted X-rays corresponds to the energy between the shells. Since the electronic shell structure of each element is specific, the X-rays or fluorescence will have characteristic energies. Hence, by measuring the intensity and energy of the fluorescence, the composition of the sample can be determined.

Figure 4.10 presents an electrodeposition experiment of Sn into NP-AAO studied *in situ* using XRF. The experiment is illustrated in Figure 4.10 (a). While Sn was

electrodeposited into the NP-AAO, the sample height was scanned through the 29.4 keV X-ray beam. The X-ray excited the atoms and electrons from the K-shell of Sn (29.2 keV) were ejected, and the resulting fluorescence intensity was measured. In Figure 4.10 (b) is the fluorescence intensity plotted against sample height for several height scans during 30 min of deposition. The increase of the intensity below the sample surface with time corresponds to an increasing amount of electrodeposited Sn into the pores.

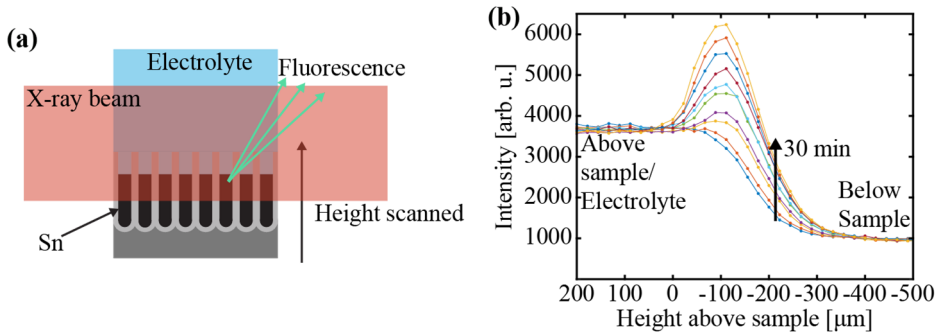

Figure 4.10: Electrodeposition of Sn into NP-AAO studied *in situ* with XRF. (a) Illustration of the experiment. While Sn was electrodeposited into the pores, the height of the sample was scanned through the X-ray beam. (b) The intensity of the fluorescence was recorded during the scan several times during the deposition. The fluorescence signal increases with time due to the increasing amount of Sn in the pores.

4.1.7 X-ray photoelectron spectroscopy (XPS)

X-ray photoelectron spectroscopy (XPS) is one of the most powerful surface sensitive technique used for studies of the electronic structure and chemical analysis of solids [116, 117]. Today, the technique is mature and is used both in academia and in industry.

The technique makes use of the photoelectric effect, i.e. when light is shined onto a material, electrons are emitted due to photons being absorbed by the atoms in the material. The energy of the emitted photoelectron is given by $hv - E_b - \Phi$, where hv is the photon energy, E_b is the binding energy of the photoelectron (referred to the Fermi level E_f of the sample) and Φ is the work function (defined as the minimum energy required to remove an electron from the surface to the infinity) of the sample, see Figure 4.11.

In reality, the photoelectrons are measured using a spectrometer, where the energy of the photoelectron measured by the spectrometer E_{kin} is given by equation (4.17).

The measured kinetic energy E_{kin} depend on the work function of the spectrometer Φ_{sp} as the work function of the sample cancels.

$$E_{kin} = h\nu - E_b - \Phi - (\Phi_{sp} - \Phi) = h\nu - E_b - \Phi_{sp} \qquad (4.17)$$

As the photon energy $h\nu$ and the spectrometer work function Φ_{sp} is constant (as the spectrometer is kept in UHV) and easily compensated by for example measurements of the Fermi level, the binding energy E_b of the photoelectrons can be obtained by the measurements of the kinetic energy E_{kin} of the photoelectrons.

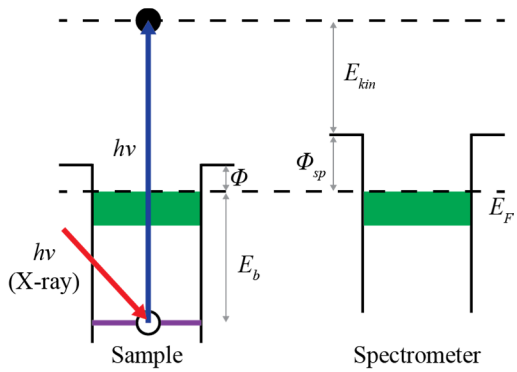

Figure 4.11: Illustration of the photoemission excitation process. An X-ray photon is absorbed by an atom and a photoelectron from a core level or valence level with binding energy E_b is emitted. The kinetic energy E_{kin} measured by the spectrometer is the x-ray photon energy subtracted by the binding energy and the work function of the spectrometer. Adapted from [117].

An XPS measurement is commonly performed by shining with a monochromatic X-ray beam onto the sample and simultaneously measure the intensity of photoelectrons at different energies by scanning the energy which is detected continuously. The resulting spectrum is plotted as a function of the binding energy E_b, where core level peaks from the different elements in the sample can be identified. From the position of the peaks and since each element have their energy levels at their own specific energies, it is possible to perform element analysis. Further, since the energy levels are shifted (usually 1-10 eV) depending on the environment, it is possible to determine the chemical environment from the shifts of the peaks, e.g. to determine the oxidation states present in the sample. Figure 4.12 shows two spectra measured from an Al(111) surface that have been oxidized by exposure to O_2. The oxide give rise to additional peaks (Al $2p_{ox}$) in the Al 2p spectrum that have higher binding energies than the peaks originating from Al in the metal (Al $2p_{3/2,1/2}$). In addition, the O in the oxide give rise to the peak in the O 1s spectrum.

The integrated intensity of the peaks can also be used for quantitative analysis, e.g. determine the amount of each element in the material. To do this one needs to take into account the photoemission probability from the elements at a given energy, the so-called photoelectron cross-section.

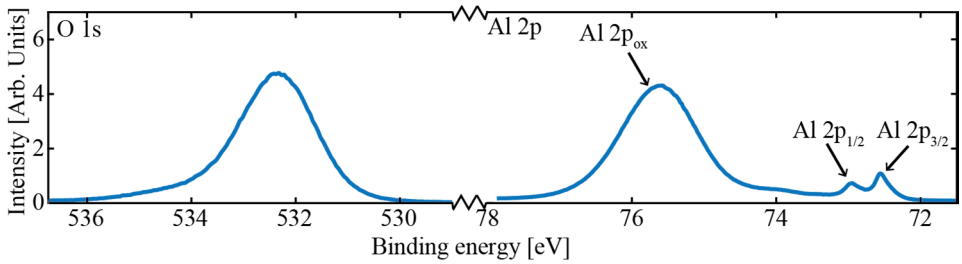

Figure 4.12: O 1s and Al 2p spectra measured of an oxidized Al(111) surface.

In the present thesis, we have from Al 2p spectra quantitatively determined the thickness of the native oxide films on Al single crystals as well as on aluminum alloys by approximating the oxide as a homogeneous layer on top of a homogeneous Al substrate. For such a model, the thickness d_{xps} is determined using equation (4.18), where I is the intensity of the peaks, N is the density of Al atoms, λ is the electron inelastic mean free path and Θ is the photoelectron emission angle. The subscription me and ox corresponds to metal and oxide, respectively.

$$d_{xps} = \lambda_{ox} sin\Theta \ln\left(\frac{N_{me}\lambda_{me}I_{ox}}{N_{ox}\lambda_{ox}I_{me}}\right) \quad (4.18)$$

4.2 Electrochemical methods

Electrochemical methods are based on either measuring the potential difference between the electrodes in the electrochemical cell or the current passing between the electrodes [57]. In the present thesis, electrochemical measurements were performed to determine the process or reactions occurring at the electrodes as well as the morphology and electrochemical resistance of native and anodic oxides.

A first determination of the electrochemical properties of the electrode (sample) is obtained by measuring the open-circuit potential (OCP) between the working and reference electrode in the electrochemical cell. When an electrode is immersed in an electrolyte, anodic and cathodic reactions occur at the electrode interfaces which shifts the electrode potential. The potential stabilizes at the OCP where the transfer

rates of the anodic and cathodic reactions are equal. The value of the OCP is strongly affected by the alloying elements existing in the solid solution, but not much by the intermetallic particles [2]. Elements such as Cu, Mn and Si are known to shift the OCP in the nobler/positive direction, and Mg and Zn to the active/negative direction. A higher nobility of a material can be an indication of a higher corrosion resistance, but this is not always the case as a higher amount of alloying elements also results in an increasing amount of heterogeneities, in the shape of intermetallic particles, that instead lowers the corrosion resistance [2].

When the potential is kept constant, as during potentiostatic anodization, it is possible from the measured current to determine the amount of reactions that have occurred at the electrodes. In section (3.2.3) about anodization, it was also shown that the measured current transient could be used to determine the morphology of the growing anodic oxide, i.e. barrier- or porous-type oxide film.

The behavior of the electrochemical system can also be studied by varying the potential in a systematic manner and measure the response current or vice versa. A popular method in which this is used is cyclic voltammetry (CV), where the potential of the working electrode is linearly ramped to a potential and then linearly ramped back again. During the ramping a variety processes can occur at different potentials during the ramp, which is seen as peaks in the current. Examples of processes are adsorption and desorption of electrolyte species, oxide formation, hydrogen evolution, and oxygen evolution [57]. Another technique where also the system is probed in a controlled manner is electrochemical impedance spectroscopy (EIS). This electrochemical method was extensively used in the present thesis and is further described below.

4.2.1 Electrochemical impedance spectroscopy (EIS)

Electrochemical impedance spectroscopy (EIS) is a method where the electrical properties of electrochemical systems are studied. Information regarding, for example, corrosion and microstructural properties are possible to obtain from the sample, i.e. one of the electrodes. The method can be performed *in situ* in aqueous environments and is usually regarded as non-destructive. The technique has been available for several decades, and more in-depth descriptions can be found in, for example, refs. [118, 119].

An EIS measurement is commonly performed by applying many small amplitude sinusoidal potentials, with different frequencies, across the electrochemical system and measure the corresponding current response at the same frequency. From the potential $E(t)$ and the current $I(t)$, the impedance $Z(\omega)$ of the system can be obtained:

$$Z(\omega) = \frac{E(t)}{I(t)} = \frac{E_0 \sin(\omega t)}{I_0 \sin(\omega t + \theta)} = Z'(\omega) + jZ''(\omega) \quad (4.19)$$

where $\omega = 2\pi f$ is the angular frequency (where f is the frequency), E_0 is the amplitude of the potential, I_0 is the amplitude of the current, t is the time and θ is the phase shift between the excitation potential and the current response. Using Euler's formula, the impedance can be expressed as a complex function that consists of a real part $Z'(\omega)$ and an imaginary part $Z''(\omega)$. The resulting spectrum from the measurement at different frequencies are commonly plotted in two different ways, in Figure 4.13 (a-b) as the Bode modulus ($Z(\omega)$ vs. f) and the Bode phase plot (Phase vs. f) or in Figure 4.13 (c) as a Nyquist plot (Z'' vs. Z').

To analyze the data, the spectrum is fitted to an electrical circuit model that is equivalent to the electrochemical system. The data shown as an example in Figure 4.13 (a-c) consist of one peak in the Bode phase plot and one semicircle in the Nyquist plot. This means the system can be well described by the equivalent circuit in Figure 4.13 (d), where R_s is the solution resistance, R_p is the polarization resistance and CPE is the constant phase element. The CPE impedance function $Z_{CPE} = 1/[Y_0(j\omega)^n]$, where Y_0 is a constant. If $n = 1$ the CPE element acts as pure capacitor.

In the present thesis, we have studied aluminum oxide films on aluminum substrates using EIS where the equivalent circuit shown in Figure 4.13 (d) were often used for the analysis. With the approximation that the capacitance obtained from the CPE element is due to the oxide, the thickness of the oxide film can be estimated. To obtain the thickness, the oxide is modelled as a parallel plate capacitor with the capacitance

$$C = \frac{\varepsilon_0 \varepsilon_r A}{d} \quad (4.20)$$

where ε_0 is the dielectric permittivity in vacuum, ε_r is the dielectric constant of the oxide, A is the effective surface area, and d is the thickness of the oxide layer. The accuracy of the estimated thickness relies, for instance, on the accuracy at which the dielectric constant and the effective area can be determined. The effective area can be approximated with a macroscopic area of the surface. This approximation improves if the surface is well polished. For aluminum oxides, a large range of dielectric constants (7.5-15) have been reported, which limits the accuracy if this constant is not known. Compared to thickness estimations using XRR, the accuracy of EIS appears to be less accurate in the case of flat surfaces with little roughness. However, EIS is superior for rougher surfaces as it is still possible to obtain a thickness estimation sufficiently accurate for relative thickness determinations.

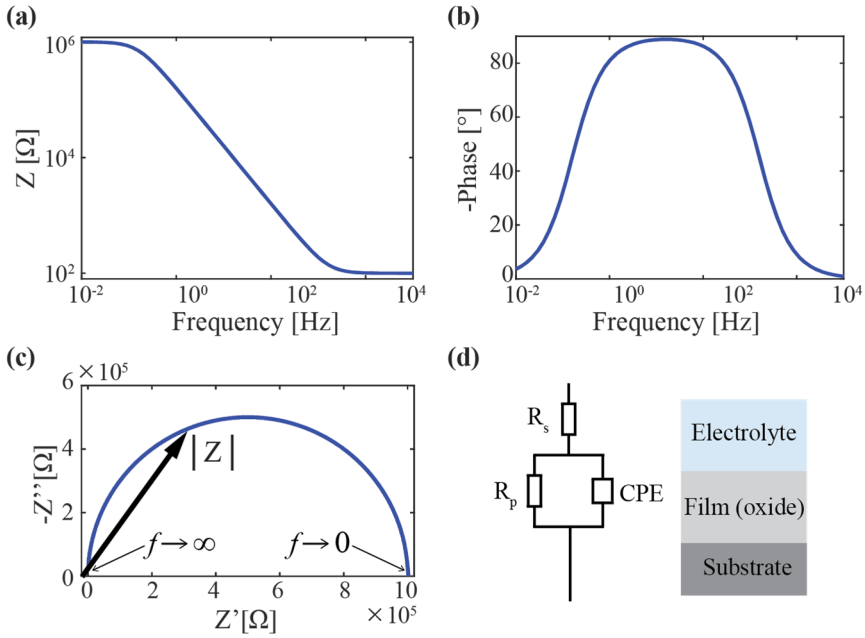

Figure 4.13: EIS data represented in (a-b) as Bode modulus and Bode phase plot and in (c) as Nyquist plot. Panel (d) shows the equivalent circuit describing the data in (a-c) well. Adapted from [119].

4.3 Microscopy

In the present thesis, Scanning Electron Microscopy (SEM) and Atomic Force Microscopy (AFM) have been used to characterize the surface topography and morphology of aluminum oxides *ex situ*. In SEM, the probe consists of a focused beam of high-energy electrons that is raster scanned over the surface. When the electrons hit the surface, they can either be backscattered elastically or scatter inelastically, resulting in the emission of secondary electrons [120]. The contrast in the image is achieved by measuring the intensity of either the backscattered electrons or the secondary electrons while the electron beam is scanned across the surface. In the present thesis, we used the secondary electrons to obtain a topographic contrast of the sample surface.

In AFM, it is instead a cantilever with a sharp tip that is raster scanned over the surface [121]. The contrast is achieved by measuring how much the cantilever is deflected while scanning over the surface. In the present thesis, the deflection is detected by measuring the intensity of a laser that is reflected on the cantilever.

Forces on the tip are caused by Van der Waals interactions and Pauli repulsions between the tip and the surface, which are either attractive or repulsive depending on the distance between the tip and the surface. Two different AFM modes were used for the studies. In contact mode, the distance between the cantilever and the surface is a few Å, and the force between the tip and the surface is kept constant. In tapping mode, the distance between the tip and surface is tens to hundreds of Å. The cantilever is kept oscillating at its resonance frequency, where the contrast is due to the measured change in amplitude, phase or frequency. Changes in the amplitude are used to achieve topographic resolution.

SEM and AFM have advantages and disadvantages. The SEM is usually faster and easier to use, while difficulties arise when attempting to study non-conducting samples, as thicker aluminum oxides, due to charging. However, AFM does not have this limitation and also thicker oxides can be measured. It is also possible to obtain a higher resolution with AFM.

4.4 Setups for *in situ* studies

For most of the studies in the present thesis, a custom made electrochemical cell in two different setups has been used, which allows for *in situ* studies of anodization with electrochemical and X-ray scattering methods. The first section (4.4.1) describes the setup used for the combined studies with electrochemical methods and XRR. The second section (4.4.2) describes the setup used for studies of NP-AAO with GTSAXS and XRF. The electrochemical cell that was used in both setups will be described in the first section.

4.4.1 Setup for *in situ* anodization studies with both electrochemical methods and XRR

Figure 4.14 (a) and (b) shows a photo and an illustration of the electrochemical cell and (c) a schematic of the setup with the cell viewed in cross section. The cell is similar to the cell described in ref. [122]. The cell body is made of polyether ether ketone (PEEK) and have an inner cylindrical volume of 2-3 ml and a diameter of 8 mm for the electrolyte. The cell has two openings on the side for the inlet and outlet of the electrolyte. A three electrode setup was employed for the experiments. A hat shaped sample was used as the working electrode and was inserted from the bottom. A glassy carbon rod was used as counter electrode and was inserted from the top. A miniature Ag/AgCl reference electrode was inserted from the side with the end positioned in between the counter and the working electrode. Two larger PEEK caps

were screwed onto the bottom and top of the cell. The top and bottom openings were sealed by the use of silicone washers between the base of the hat-shaped sample and the cell as well as between the top cap and the cell. The other openings were sealed by viton o-rings around the electrodes, which were pressed against the cell and the top cap by smaller plastic screws.

The inlet of the cell was connected to pressurized bottles with electrolyte or water. Exchange of electrolyte was done by opening valves to the bottles which forced electrolyte to flow through the cell.

During the experiments, the anodization and the electrochemical measurements were controlled using a potentiostat. The X-ray beam entered the cell through the 0.1 mm thin walls at the neck of the cell and was reflected on the sample surface. The incidence angle was changed during the measurements by tilting the cell with the sample, and the detector was moved correspondingly to measure the specular reflected X-ray beam.

The cell is generally robust. The sample can be exchanged quickly allowing for several samples to be measured during an experimental session at synchrotrons, i.e. beamtimes. Another advantage is that the electrolyte is exchanged without the need of moving the cell, which facilities continuous *in situ* experiments without major realignments of the sample to the X-ray beam. It also makes it possible to perform experiments where the liquid environment needs to be exchanged quickly. The electrolyte can also be exchanged without the sample getting in contact with atmosphere.

A large drawback with the cell is that the side of the sample and not only the top surface is in contact with the electrolyte. This has large consequences for the electrochemical measurements as the sides will contribute to the measurements. This is especially a large disadvantage when measuring well defined polished single crystal surfaces since the side can be much different from the single crystal surface. However, it is not as important when measuring polycrystalline aluminum or aluminum alloys substrates where the polished surface is not very well defined and similar to the sides. The effect of the sides does not influence the XRR measurement since the X-ray beam only probes the top surface of the sample.

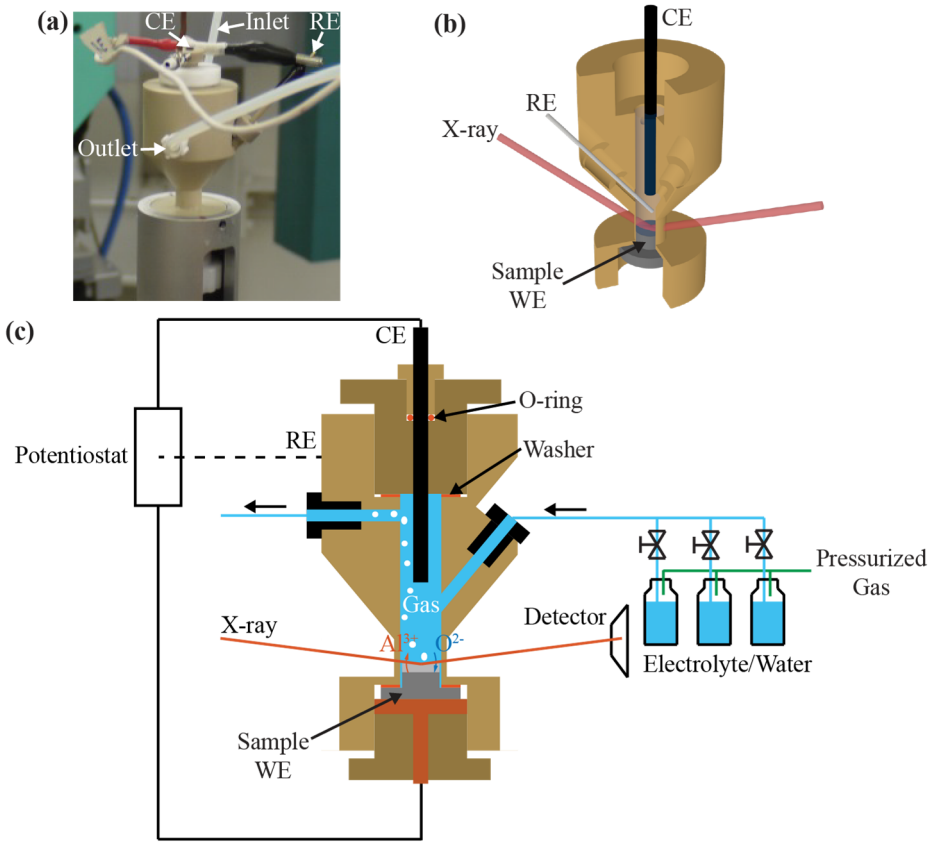

Figure 4.14: The setup used for *in situ* anodization studies with electrochemical methods and XRR combined. (a) Photo of the cell. (b) Illustration of the cell with a removed section revealing the inside. (c) Schematics of the setup with the cell viewed in cross section. RE: reference electrode, CE: counter electrode, WE: working electrode.

4.4.2 Setup for *in situ* anodization of NP-AAO studied with GTSAXS and XRF

For the GTSAXS and XRF studies of NP-AAO, the same cell as above was used. However, the setup needed to be modified due to the harsher anodization conditions where a huge amount of gas is formed and since the electrolyte needed to be cooled for the NP-AAO growth and heated for the pore widening. The setup used is shown schematically in Figure 4.15. A two-electrode setup was employed, and a thermocouple was inserted instead of the reference electrode to measure the temperature in the cell. The removal of gas and the cooling/heating of the electrolyte in the cell were achieved by continuously circulating cooled/heated electrolyte through the cell with a peristaltic pump. The anodization potential was in this setup controlled by a power supply. The robustness of the cell and the ease at which the electrolyte environment can be changed facilitated the electrolytic deposition experiments as all the process steps, i.e. anodization, pore widening, barrier layer thinning and electrolytic deposition could be performed in one continuous running experiment without removing the cell.

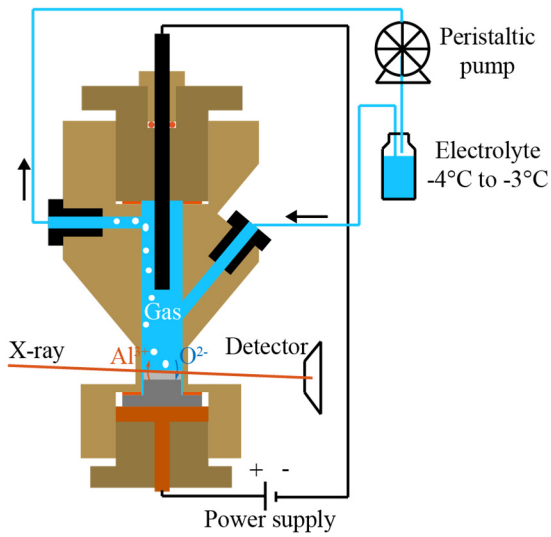

Figure 4.15: The setup used for *in situ* anodization studies of NP-AAO with GTSAXS and XRF.

5 Conclusions and outlook

A large part of my work during my PhD has been on improving the infrastructure to be able to perform electrochemistry at the division of synchrotron radiation research as well as at synchrotrons. From being in principle non-existing at the division, a huge step has been taken, and today the equipment and the setups needed to perform state of the art *in situ* electrochemistry research are available. The possibility of bringing our setup also increases the number of beamlines at synchrotrons where we can perform the experiments. During my PhD, successful experiments have been performed at the synchrotron facilities MAX IV, ESRF, Diamond, APS, and Petra III. The possibility of also being able to prepare experiments in the home lab before the synchrotron measurements is an enormous advantage. I expect that the possibilities of doing electrochemistry at the division will be further improved in the future.

During the experiments, the electrochemical growth of anodic oxides was mostly studied. The anodization of both fundamental single crystal surface model systems, as well as aluminum alloys used for applications, have successfully been studied *in situ* at synchrotrons simultaneously with XRR and EIS. However, the corrosion resistance and stability of these oxides have not been equally much studied. Corrosion is an extremely important field, not only for aluminum but also for other materials such as steel. A natural and possible step forward would be to apply the approach of using X-ray and electrochemical methods simultaneously to improve the knowledge and shed new light on corrosion processes on aluminum and other materials.

NP-AAO is one of the most interesting materials for future nanotechnology and is studied by many groups around the world. We have been able to follow the self-organization of the pores with unique temporal resolution using the newly introduced technique GTSAXS and the difference between profiles approach. The use of this method could be a tool for improving the understanding of the pore formation and self-organization, which today is not fully known. For example, it could be of interest to measure the self-organization of the pores during anodization with GTSAXS when different amount of stress is applied to the material.

Further, the approach of studying these periodic structures using GTSAXS opens the door for *in situ* studies of realistic industrial processes since the periodic pores could be used as models for electrolytic coloring and corrosion studies. In

accordance with that direction, we also did successful measurements of electrolytic coloring with Sn, where XRF was used in addition to GTSAXS.

There are many possible applications of NP-AAO such as for catalysis, filtering, batteries and solar cells. A possible step in the future would be to use our approach for studies of both the production and function of these NP-AAO based applied materials. In particular, the electrochemical deposition of catalytic active materials inside the pores is of interest, especially if the NP-AAO is used as a membrane, through which the reactants and products can flow.

In the present thesis, mainly aluminum was considered, but other metals, such as Ti, can also form self-ordered oxide structures when anodized. In the future, it could also be of interest to study these metals with our approach.

The possibilities of upgraded or new synchrotrons such as MAX IV will provide in the future are tremendous. One of the interesting properties of these synchrotrons is the high coherence and small nano-sized X-ray beam they will provide. Corrosion of aluminum is a local effect occurring due to the heterogeneous microstructure of the material. With a nanobeam that is smaller than the micro-sized intermetallic particles, it should be possible to follow the corrosion process around these particles *in situ* as it occurs using methods such as nano-XRF, nano-XRD, or even coherent diffraction imaging and ptychography.

The nanobeams would also be suitable for studies of NP-AAO and could shed new light on the pore formation and self-organization as well as be used for studies of functional nanodevices in the NP-AAO. In particular, a number of functionalization processes such as electrodeposition and coloring could be studied *in situ* on a nanoscale by nano-XRF and nano-XRD mapping.

To summarize, during my PhD we have initiated research regarding electrochemistry at the division. Especially, the anodization of aluminum has *in situ* been studied on both fundamental single crystal surfaces and applied aluminum alloys. The studies have been performed in a unique fashion were both electrochemical, and state of the art synchrotron-based X-ray methods have been combined for the characterization of the anodic oxides. I am convinced that the work at the division will continue, possible also in a more fundamental direction, as well as with other methods such as laser characterization techniques.

6 References

1. Lee, W. and S.-J. Park, *Porous Anodic Aluminum Oxide: Anodization and Templated Synthesis of Functional Nanostructures.* Chemical Reviews, 2014. **114**(15): p. 7487-7556.

2. Sukiman, N.L., et al., *Durability and Corrosion of Aluminium and Its Alloys: Overview, Property Space, Techniques and Developments*. Aluminium Alloys - New Trends in Fabrication and Applications. 2012: InTech.

3. Diggle, J.W., T.C. Downie, and C.W. Goulding, *Anodic oxide films on aluminum.* Chemical Reviews, 1969. **69**(3): p. 365-405.

4. Thompson, G.E., et al., *Anodizing of aluminium alloys.* Aircraft Engineering and Aerospace Technology, 1999. **71**(3): p. 228-238.

5. Evertsson, J., et al., *The thickness of native oxides on aluminum alloys and single crystals.* Applied Surface Science, 2015. **349**(0): p. 826-832.

6. Cabrera, N. and N.F. Mott, *Theory of the Oxidation of Metals.* Reports on Progress in Physics, 1948. **12**: p. 163-184.

7. Fehlner, F.P. and N.F. Mott, *Low-temperature oxidation.* Oxidation of Metals, 1970. **2**(1): p. 59-99.

8. Masuda, H. and K. Fukuda, *Ordered Metal Nanohole Arrays Made by a Two-Step Replication of Honeycomb Structures of Anodic Alumina.* Science, 1995. **268**(5216): p. 1466-1468.

9. Masuda, H. and M. Satoh, *Fabrication of Gold Nanodot Array Using Anodic Porous Alumina as an Evaporation Mask.* Japanese Journal of Applied Physics, 1996. **35**(1B): p. L126.

10. Chun, H., et al., *Engineering Low-Aspect Ratio Carbon Nanostructures: Nanocups, Nanorings, and Nanocontainers.* ACS Nano, 2009. **3**(5): p. 1274-1278.

11. Berganza, E., et al., *Domain wall pinning in FeCoCu bamboo-like nanowires.* 2016. **6**: p. 29702.

12. Pellin, M.J., et al., *Mesoporous catalytic membranes: Synthetic control of pore size and wall composition.* Catalysis Letters, 2005. **102**(3): p. 127-130.

13. Gowda, S.R., et al., *Building Energy Storage Device on a Single Nanowire.* Nano Letters, 2011. **11**(8): p. 3329-3333.

14. McConville, C.F., et al., *Synchrotron radiation core level photoemission investigation of the initial stages of oxidation of Al(111).* Surface Science, 1987. **188**(1–2): p. 1-14.

15. Brune, H., et al., *Surface migration of ``hot'' adatoms in the course of dissociative chemisorption of oxygen on Al(111).* Physical Review Letters, 1992. **68**(5): p. 624-626.

16. Berg, C., et al., *Observation of a low-binding-energy peak in the 2p core-level photoemission from oxidized Al(111).* Physical Review B, 1993. **47**(19): p. 13063-13066.

17. Jeurgens, L.P.H., et al., *Determination of thickness and composition of aluminium-oxide overlayers on aluminium substrates.* Applied Surface Science, 1999. **144–145**: p. 11-15.

18. Schmid, M., et al., *Oxygen adsorption on Al(111): low transient mobility.* Surface Science, 2001. **478**(3): p. L355-L362.

19. Snijders, P.C., L.P.H. Jeurgens, and W.G. Sloof, *Structure of thin aluminium-oxide films determined from valence band spectra measured using XPS.* Surface Science, 2002. **496**(1–2): p. 97-109.

20. Starodub, D., T. Gustafsson, and E. Garfunkel, *The reaction of O2 with Al(1 1 0): a medium energy ion scattering study of nano-scale oxidation.* Surface Science, 2004. **552**(1–3): p. 199-214.

21. Cai, N., et al., *Tuning the Limiting Thickness of a Thin Oxide Layer on Al(111) with Oxygen Gas Pressure.* Physical Review Letters, 2011. **107**(3): p. 035502.

22. Cai, N., et al., *Effect of oxygen gas pressure on the kinetics of alumina film growth during the oxidation of Al(111) at room temperature.* Physical Review B, 2011. **84**(12): p. 125445.

23. Cai, N., et al., *Comparative Study of the Passivation of Al(111) by Molecular Oxygen and Water Vapor.* The Journal of Physical Chemistry C, 2013. **117**(1): p. 172-178.

24. Cai, N., et al., *X-ray Photoelectron Spectroscopy Study of the Passivation of NiAl(100) by Water Vapor.* Langmuir, 2014. **30**(3): p. 774-783.

25. Kresse, G., et al., *Structure of the Ultrathin Aluminum Oxide Film on NiAl(110).* Science, 2005. **308**(5727): p. 1440-1442.

26. Martin, N.M., et al., *High-resolution core-level spectroscopy study of the ultrathin aluminum oxide film on NiAl(110).* Physical Review B, 2011. **83**(12): p. 125417.

27. Prévot, G., et al., *Sixton rectangles in the structure of alumina ultrathin films on metals.* Physical Review B, 2010. **81**(8): p. 085405.

28. Prévot, G., et al., *Archetypal structure of ultrathin alumina films: Grazing-incidence x-ray diffraction on Ni(111).* Physical Review B, 2012. **85**(20): p. 205450.

29. Schmid, M., et al., *Nanotemplate with Holes: Ultrathin Alumina on Ni3Al(111).* Physical Review Letters, 2007. **99**(19): p. 196104.

30. Hasnaoui, A., et al., *Nanoscale oxide growth on Al single crystals at low temperatures: Variable charge molecular dynamics simulations.* Physical Review B, 2006. **73**(3): p. 035427.

31. Baran, J.D., H. Grönbeck, and A. Hellman, *Mechanism for Limiting Thickness of Thin Oxide Films on Aluminum.* Physical Review Letters, 2014. **112**(14): p. 146103.

32. Levin, I. and D. Brandon, *Metastable Alumina Polymorphs: Crystal Structures and Transition Sequences.* Journal of the American Ceramic Society, 1998. **81**(8): p. 1995-2012.

33. Digne, M., et al., *Structure and Stability of Aluminum Hydroxides: A Theoretical Study.* The Journal of Physical Chemistry B, 2002. **106**(20): p. 5155-5162.

34. Digne, M., et al., *Use of DFT to achieve a rational understanding of acid–basic properties of γ-alumina surfaces.* Journal of Catalysis, 2004. **226**(1): p. 54-68.

35. Krokidis, X., et al., *Theoretical Study of the Dehydration Process of Boehmite to γ-Alumina.* The Journal of Physical Chemistry B, 2001. **105**(22): p. 5121-5130.

36. Mansfeld, F. and M.W. Kendig, *Evaluation of Anodized Aluminum Surfaces with Electrochemical Impedance Spectroscopy.* Journal of The Electrochemical Society, 1988. **135**(4): p. 828-833.

37. Skeldon, P., et al., *A Tracer Study of Porous Anodic Alumina.* Electrochemical and Solid-State Letters, 2006. **9**(11): p. B47-B51.

38. Garcia-Vergara, S.J., et al., *A flow model of porous anodic film growth on aluminium.* Electrochimica Acta, 2006. **52**(2): p. 681-687.

39. Oh, J. and C.V. Thompson, *The role of electric field in pore formation during aluminum anodization.* Electrochimica Acta, 2011. **56**(11): p. 4044-4051.

40. Zhang, F., J.-O. Nilsson, and J. Pan, *In Situ and Operando AFM and EIS Studies of Anodization of Al 6060: Influence of Intermetallic Particles.* Journal of The Electrochemical Society, 2016. **163**(9): p. C609-C618.

41. Davoodi, A., et al., *In Situ Investigation of Localized Corrosion of Aluminum Alloys in Chloride Solution Using Integrated EC-AFM/SECM Techniques.* Electrochemical and Solid-State Letters, 2005. **8**(6): p. B21-B24.

42. Davoodi, A., et al., *The Role of Intermetallic Particles in Localized Corrosion of an Aluminum Alloy Studied by SKPFM and Integrated AFM/SECM.* Journal of The Electrochemical Society, 2008. **155**(5): p. C211-C218.

43. Davoodi, A., et al., *An insight into the influence of morphological and compositional heterogeneity of an individual intermetallic particle on aluminium alloy corrosion initiation.* Materials and Corrosion, 2013. **64**(3): p. 195-198.

44. Gustafson, J., et al., *High-Energy Surface X-ray Diffraction for Fast Surface Structure Determination.* Science, 2014. **343**(6172): p. 758-761.

45. Essehli, R., et al., *Structural changes upon lithium insertion in Ni0.5TiOPO4.* Journal of Alloys and Compounds, 2012. **530**: p. 178-185.

46. Ferrer, S., M.D. Ackermann, and E. Lundgren, *In Situ Investigations of Chemical Reactions on Surfaces by X-Ray Diffraction at Atomospheric Pressures.* MRS Bulletin, 2007. **32**(12): p. 1010-1014.

47. Renner, F.U., et al., *Initial corrosion observed on the atomic scale.* Nature, 2006. **439**(7077): p. 707-710.

48. Stamenkovic, V.R., et al., *Improved Oxygen Reduction Activity on Pt₃Ni(111) via Increased Surface Site Availability.* Science, 2007. **315**(5811): p. 493-497.

49. Lucas, C.A., et al., *From ultra-high vacuum to the electrochemical interface: X-ray scattering studies of model electrocatalysts.* Faraday Discussions, 2009. **140**(0): p. 41-58.

50. Lucas, C.A., et al., *The structure of the electrochemical double layer: Ag(111) in alkaline electrolyte.* Electrochemistry Communications, 2011. **13**(11): p. 1205-1208.

51. Gründer, Y. and C.A. Lucas, *Surface X-ray diffraction studies of single crystal electrocatalysts.* Nano Energy, 2016. **29**(Supplement C): p. 378-393.

52. *SSF Program ALUminium oXides for processing and products ALUX*. [cited 2016; Available from: http://www.alux.lu.se/.

53. Kittel, C., *Introduction to Solid State Physics*. 8th ed. 2004: John Wiley & Sons.

54. Easton, M.A. and D.H. StJohn, *Improved prediction of the grain size of aluminum alloys that includes the effect of cooling rate.* Materials Science and Engineering: A, 2008. **486**(1–2): p. 8-13.

55. *Wrought Aluminum International Alloy Designations & Chemical Composition Limits*. [cited 20160127; Available from: http://www.aluminum.org/.

56. Zoski, C.G., *Handbook of Electrochemistry*. 2007: Elsevier.

57. Bard, A.J. and L.R. Faulkner, *Electrochemical Methods: Fundamentals and Applications*. 2nd Edition ed. 2001: John Wiley & Sons, Inc.

58. McCafferty, E., *Introduction to Corrosion Science.* 2010: New York, NY : Springer New York, 2010.

59. Sato, N., *An overview on the passivity of metals.* Corrosion Science, 1990. **31**(Supplement C): p. 1-19.

60. Szklarska-Smialowska, Z., *Mechanism of pit nucleation by electrical breakdown of the passive film.* Corrosion Science, 2002. **44**(5): p. 1143-1149.

61. Lohrengel, M.M., *Thin anodic oxide layers on aluminium and other valve metals: high field regime.* Materials Science and Engineering: R: Reports, 1993. **11**(6): p. 243-294.

62. Atkinson, A., *Transport processes during the growth of oxide films at elevated temperature.* Reviews of Modern Physics, 1985. **57**(2): p. 437-470.

63. Momma, K. and F. Izumi, *VESTA 3 for three-dimensional visualization of crystal, volumetric and morphology data.* Journal of Applied Crystallography, 2011. **44**(6): p. 1272-1276.

64. Hashimoto, H., et al., *NMR Spectroscopic Analysis of the Local Structure of Porous-Type Amorphous Alumina Prepared by Anodization.* The Journal of Physical Chemistry C, 2017. **121**(22): p. 12300-12307.

65. Farnan, I., et al., *Structural chemistry of anodic alumina.* Thin Solid Films, 1989. **173**(2): p. 209-215.

66. Llewelyn Leach, J.S. and B.R. Pearson, *The effect of foreign ions upon the electrical characteristics of anodic ZrO2 films.* Electrochimica Acta, 1984. **29**(9): p. 1271-1282.

67. Thompson, G.E. and G.C. Wood, *Porous anodic film formation on aluminium.* Nature, 1981. **290**(5803): p. 230-232.

68. Houser, J.E. and K.R. Hebert, *The role of viscous flow of oxide in the growth of self-ordered porous anodic alumina films.* Nat Mater, 2009. **8**(5): p. 415-420.

69. Cheng, C. and A.H.W. Ngan, *Theoretical Pore Growth Models for Nanoporous Alumina*, in *Nanoporous Alumina: Fabrication, Structure, Properties and Applications*, D. Losic and A. Santos, Editors. 2015, Springer International Publishing: Cham. p. 31-60.

70. 海老原, 健., 英. 高橋, and 政. 永山, *シュウ酸中で生成したポーラス型アルミニウムアノード酸化皮膜の構造と密度.* 金属表面技術, 1983. **34**(11): p. 548-553.

71. Lee, W., et al., *Fast fabrication of long-range ordered porous alumina membranes by hard anodization.* Nat Mater, 2006. **5**(9): p. 741-747.

72. Bernard, W.J. and J.W. Cook, *The Growth of Barrier Oxide Films on Aluminum.* Journal of The Electrochemical Society, 1959. **106**(8): p. 643-646.

73. Dorsey, G.A., *Some Evidence for Duplex Film Structuring Within the Anodic Alumina Barrier Layer.* Journal of The Electrochemical Society, 1969. **116**(4): p. 466-471.

74. Schultze, J.W. and M.M. Lohrengel, *Stability, reactivity and breakdown of passive films. Problems of recent and future research.* Electrochimica Acta, 2000. **45**(15–16): p. 2499-2513.

75. Masuda, H., et al., *Highly ordered nanochannel-array architecture in anodic alumina.* Applied Physics Letters, 1997. **71**(19): p. 2770-2772.

76. Passaglia, E., R.R. Stromberg, and J. Kruger, *Ellipsometry in the Measurement of Surfaces and Thin Films: Symposium Proceedings*. 1964: U.S. National Bureau of Standards.

77. Plumb, R.C., *Studies of the Anodic Behavior of Aluminum: II . Coulometry of Barrier Layer Production.* Journal of The Electrochemical Society, 1958. **105**(9): p. 498-502.

78. Renshaw, T.A., *A Study of Pore Structures on Anodized Aluminum.* Journal of The Electrochemical Society, 1961. **108**(2): p. 185-191.

79. Hunter, M.S. and P.F. Towner, *Determination of the Thickness of Thin Porous Oxide Films on Aluminum.* Journal of The Electrochemical Society, 1961. **108**(2): p. 139-144.

80. Wernick, S., R. Pinner, and P.G. Sheasby, *The surface treatment and finishing of aluminium and its alloys*. 1987: Ohio : ASM International, 1987

5. ed.

81. O'Sullivan, J.P. and G.C. Wood, *The Morphology and Mechanism of Formation of Porous Anodic Films on Aluminium.* Proceedings of the Royal Society of London. A. Mathematical and Physical Sciences, 1970. **317**(1531): p. 511-543.

82. Thompson, G.E., *Porous anodic alumina: fabrication, characterization and applications.* Thin Solid Films, 1997. **297**(1–2): p. 192-201.

83. Baron-Wiecheć, A., et al., *Tracer study of pore initiation in anodic alumina formed in phosphoric acid.* Electrochimica Acta, 2013. **113**: p. 302-312.

84. Li, F., L. Zhang, and R.M. Metzger, *On the Growth of Highly Ordered Pores in Anodized Aluminum Oxide.* Chemistry of Materials, 1998. **10**(9): p. 2470-2480.

85. Sato, N., *A theory for breakdown of anodic oxide films on metals.* Electrochimica Acta, 1971. **16**(10): p. 1683-1692.

86. Cheng, C. and A.H.W. Ngan, *Modelling and simulation of self-ordering in anodic porous alumina.* Electrochimica Acta, 2011. **56**(27): p. 9998-10008.

87. Cheng, C. and A.H.W. Ngan, *Growth Sustainability of Nanopore Channels in Anodic Aluminum Oxide Guided with Prepatterns.* The Journal of Physical Chemistry C, 2013. **117**(23): p. 12183-12190.

88. Hebert, K.R., et al., *Morphological instability leading to formation of porous anodic oxide films.* Nat Mater, 2012. **11**(2): p. 162-166.

89. Cheng, C., *Electro-Chemo-Mechanics of Anodic Porous Alumina Nano-Honeycombs: Self-Ordered Growth and Actuation*. 2015: Springer Berlin Heidelberg.

90. Schwartz, G.C. and V. Platter, *An Anodic Process for Forming Planar Interconnection Metallization for Multilevel LSI.* Journal of The Electrochemical Society, 1975. **122**(11): p. 1508-1516.

91. Li, A.P., et al., *Hexagonal pore arrays with a 50–420 nm interpore distance formed by self-organization in anodic alumina.* Journal of Applied Physics, 1998. **84**(11): p. 6023-6026.

92. Nielsch, K., et al., *Self-ordering Regimes of Porous Alumina: The 10 Porosity Rule.* Nano Letters, 2002. **2**(7): p. 677-680.

93. AlMawlawi, D., N. Coombs, and M. Moskovits, *Magnetic properties of Fe deposited into anodic aluminum oxide pores as a function of particle size.* Journal of Applied Physics, 1991. **70**(8): p. 4421-4425.

94. Takahashi, H., et al., *The cathodic polarization of aluminum covered with anodic oxide films in a neutral borate solution—I. The mechanism of rectification.* Corrosion Science, 1994. **36**(4): p. 677-688.

95. Gerein, N.J. and J.A. Haber, *Effect of ac Electrodeposition Conditions on the Growth of High Aspect Ratio Copper Nanowires in Porous Aluminum*

Oxide Templates. The Journal of Physical Chemistry B, 2005. **109**(37): p. 17372-17385.

96. Nielsch, K., et al., *Uniform Nickel Deposition into Ordered Alumina Pores by Pulsed Electrodeposition.* Advanced Materials, 2000. **12**(8): p. 582-586.

97. Zaraska, L., et al., *Synthesis of Nanoporous Anodic Alumina by Anodic Oxidation of Low Purity Aluminum Substrates*, in *Nanoporous Alumina: Fabrication, Structure, Properties and Applications*, D. Losic and A. Santos, Editors. 2015, Springer International Publishing: Cham. p. 61-106.

98. Nobelprize.org. *Discoveries in the Field of X-rays*. Available from: http://www.nobelprize.org/educational/physics/x-rays/discoveries-1.html.

99. Als-Nielsen, J. and D. McMorrow, *Elements of Modern X-ray Physics*. 2nd ed. 2011: John Wiley & Sons, Ltd.

100. Renaud, G., R. Lazzari, and F. Leroy, *Probing surface and interface morphology with Grazing Incidence Small Angle X-Ray Scattering.* Surface Science Reports, 2009. **64**(8): p. 255-380.

101. Feidenhans'l, R., *Surface structure determination by X-ray diffraction.* Surface Science Reports, 1989. **10**(3): p. 105-188.

102. Henke, B.L., E.M. Gullikson, and J.C. Davis, *X-Ray Interactions: Photoabsorption, Scattering, Transmission, and Reflection at E = 50-30,000 eV, Z = 1-92.* Atomic Data and Nuclear Data Tables, 1993. **54**(2): p. 181-342.

103. Gullikson, E. *X-Ray Interactions With Matter*. 1995; Available from: http://henke.lbl.gov/optical_constants/.

104. Levine, J.R., et al., *Grazing-incidence small-angle X-ray scattering: new tool for studying thin film growth.* Journal of Applied Crystallography, 1989. **22**(6): p. 528-532.

105. Lu, X., et al., *Grazing-incidence transmission X-ray scattering: surface scattering in the Born approximation.* Journal of Applied Crystallography, 2013. **46**(1): p. 165-172.

106. Förster, S., et al., *Scattering Curves of Ordered Mesoscopic Materials.* The Journal of Physical Chemistry B, 2005. **109**(4): p. 1347-1360.

107. Engel, M., et al., *Small-angle X-ray scattering (SAXS) off parallel, cylindrical, well-defined nanopores: from random pore distribution to highly ordered samples.* Applied Physics A, 2009. **97**(1): p. 99-108.

108. Seeck, O.H. and B. Murphy, *X-Ray Diffraction Modern Experimental Techniques*. 2015: Taylor & Francis Group, LLC.

109. Sardela, M., *Practical Materials Characterization*. 2014: Springer New York.

110. Holst, B. and G. Bracco, *Surface Science Techniques*. 2013: Springer Berlin Heidelberg.

111. Tolan, M., *X-ray Scattering from Soft-Matter Thin Films - Material Science and Basic Research*. 1999, Berlin, Heidelberg: Springer-Verlag.

112. Parratt, L.G., *Surface Studies of Solids by Total Reflection of X-Rays.* Physical Review, 1954. **95**(2): p. 359-369.

113. Névot, L. and P. Croce, *Caractérisation des surfaces par réflexion rasante de rayons X. Application à l'étude du polissage de quelques verres silicates.* Rev. Phys. Appl. (Paris), 1980. **15**(3): p. 761-779.

114. Bertram, F., *The structure of ultrathin iron oxide films studied by x-ray diffraction*. 2012.

115. *X-ray Fluorescence (XRF) and Particle-Induced X-ray Emission (PIXE)*, in *Atomic and Nuclear Analytical Methods: XRF, Mössbauer, XPS, NAA and B63Ion-Beam Spectroscopic Techniques*. 2007, Springer Berlin Heidelberg: Berlin, Heidelberg. p. 1-90.

116. Kumar, C.S.S.R., *Surface Science Tools for Nanomaterials Characterization*. 2015: Springer-Verlag Berlin Heidelberg.

117. Hofmann, S., *Auger- and X-Ray Photoelectron Spectroscopy in Materials Science*. 2013: Springer Berlin Heidelberg.

118. Perez, N., *Electrochemistry and Corrosion Science*. 2004: Springer US.

119. Lasia, A., *Electrochemical Impedance Spectroscopy and its Applications*. 2014: Springer New York.

120. Joy, D.C. and D.G. Howitt, *Scanning Electron Microscopy A2 - Meyers, Robert A*, in *Encyclopedia of Physical Science and Technology (Third Edition)*. 2003, Academic Press: New York. p. 457-467.

121. Eaton, P. and P. West, *Atomic Force Microscopy*. 2010: Oxford University Press.

122. Foresti, M.L., et al., *In situ X-ray analysis under controlled potential conditions: An innovative setup and its application to the investigation of ultrathin films electrodeposited on Ag(1 1 1).* Electrochimica Acta, 2006. **51**(25): p. 5532-5539.

7 Summary of papers

Paper I: *In situ anodization of aluminum surfaces studied by x-ray reflectivity and electrochemical impedance spectroscopy*

The anodization in 2 M Na_2SO_4 of Al(111) and AA 6060 samples were studied *in situ* using XRR and EIS. With both techniques, it was found that the anodic oxide film thickness increases linearly with the applied anodization potential and that the growth rate of the oxides was higher for Al(111). From the EIS measurements, it was also found for both samples that the polarization resistance increases first with the applied potential, but after a certain potential have been reached, the resistance decreased instead. Both the general resistance were higher, and the potential at which the resistance began to decrease were higher for Al(111). The decreasing resistance indicates that the barrier oxide film breaks-up and the initial formation of porous oxide. The lower break-up potential for AA 6060 was also indicated by *ex situ* SEM images. Generally, the experiments showed that valuable complementary information is obtained by the use of XRR and EIS.

Paper II: *The thickness of native oxides on aluminum alloys and single crystals*

The native oxide film thickness on several AA and Al single crystal surfaces were measured using XRR, XPS and EIS. The obtained thicknesses from XRR and XPS was in good agreement. However, the thicknesses obtained from EIS were thinner for all samples. Also, the trend between the samples was different for the thicknesses obtained from EIS than from the other two methods. Possible reasons for the discrepancy could be associated with the construction of an appropriate model used for the EIS analysis. It was also observed that the oxides on the AA were thicker than on the single crystals, which could be related to the grain structure or the alloying elements in the AA. Last, it was found that placing the samples in water increased the measured thickness.

Paper III: *Integration of electrochemical and synchrotron-based X-ray techniques for in-situ investigation of aluminum anodization*

The anodization in 1 M Na_2SO_4 of AA 6082 and AA 7075 was studied *in situ* using electrochemical methods and XRR. Compared to Paper I, both the EIS and XRR measurement was is this paper performed during the same anodization experiment instead of at two different experiments. The electrochemical analysis (current transients and EIS) of both samples indicated the formation of two-layered anodic oxides with a more compact and resistive barrier layer and a porous layer on top. The anodic oxides generally exhibited lower resistance, and the current transient was generally higher for AA 7075. After anodization at above 3 V, the thickness obtained from EIS dropped significantly for both samples and especially for AA 7075. The total thicknesses obtained from XRR increased linearly with the potential and, especially for AA 7075, the roughness increased substantially after anodization at above 3 V. The results from the combined investigation suggest that a porous-type oxide film is growing and that the barrier layer breaks after anodization above 3 V, resulting in a rougher, less resistive oxide. Importantly, the experiment shows that the combination of EIS and XRR can provide a more thorough understanding of both the electrochemical and the structural properties of the anodic oxide during anodization.

Paper IV: *Anodization of Al(100), Al(111) and Al Alloy 6063 studied in situ with X-ray reflectivity and electrochemical impedance spectroscopy*

The anodization in a neutral citrate buffer solution of Al(100), Al(111) and AA 6063 were studied using XRR and EIS. The anodic thicknesses obtained from both XRR and EIS increased with anodization potential, where the thicknesses obtained from XRR were higher. The higher thicknesses obtained from XRR are probably due to an additional porous oxide, which is not directly detected by the EIS. A two-layer model employed for the XRR analysis also suggests the two-layer porous-type oxide morphology. The thicknesses of the two-layers in the model increased similarly for all samples, but the roughness between the interfaces was higher for AA 6063. The higher roughness suggests that a higher degree of side processes occurs due to the alloying elements during anodization, which roughen the interfaces. The higher degree of side reactions or processes is also confirmed by the lower resistance obtained from EIS for the AA 6063 substrate. Compared to the anodization experiments in Na_2SO_4 (paper I & III) the fringes in the XRR curves are better defined, which is probably related to the buffer capacity that prevents lowering of the pH and, hence, dissolution processes that would have otherwise roughened the interfaces.

Paper V: *The growth and self-organisation of anodic alumina nanopores studied by time resolved X-ray scattering*

The structural evolution of NP-AAO was studied with GTSAXS during anodization in 0.3 M $C_2H_2O_4$ at 40 V. The interpore distance between pores, domain size of ordered pores and thickness of the oxide could be followed during the anodization of Al(111), Al(100) and an Al polycrystalline surface. No significant differences between the surface orientations were obtained for the interpore distance and domain length. However, a clear difference in growth rates was found. Most importantly, the paper shows that the used approach where the difference between measured GTSAXS patterns are analyzed provides a unique possibility of measuring the self-organization of the pores with an unprecedented temporal resolution.

Paper VI: *Self-organization of nanoporous aluminum oxides studied in situ with grazing-incidence transmission small-angle X-ray scattering*

The structural evolution of NP-AAO was studied with GTSAXS during anodization in 0.3 M H_2SO_4 at 25 V, and in 0.3 M $C_2H_2O_4$ at 40 V. In both electrolytes, no significant differences between the Al(100), Al(110) and Al(111) surfaces were obtained for the interpore distance and domain length. However, the interpore distance was shorter in sulfuric acid than in oxalic acid, which is expected due to the lower anodization potential used in sulfuric acid. Also, a shorter domain length was obtained in sulfuric acid. Between the surfaces and especially in oxalic acid, a clear difference in growth rates was found. It was also found that the growth rates are higher in sulfuric acid than in oxalic acid.

The effect of surface pre-patterning was also evaluated. It was found that the interpore distance in the beginning of the anodization followed that of the pre-patterning despite that it was not the optimal distance for the used anodization condition. However, as the anodization progressed, the pores reordered towards the optimal interpore distance. These experiments showed that the difference approach significantly aids the analysis, since the details of the structural changes were clearer from the difference profiles than from the as extracted profiles.

Paper VII: *In-situ X-ray observations of Sn electrodeposition into two-step anodized alumina.*

The deposition of Sn into NP-AAO was studied *in situ* using GTSAXS, XRF and XANES. With the combination, it was possible to follow the deposition process as it occurred. Changes in the GTSAXS was correlated to changes in the measured current and associated with the deposited Sn. The XANES data revealed that the deposited Sn were in the SnO_2 phase. *Ex situ* FIB-SEM images confirmed the deposition of Sn in the form of nanowires. Most important, the measurements pave the way for future *in situ* studies during electrodeposition into nanostructures such as NP-AAO. In the future, the use of smaller X-ray beams should enable an improved spatial resolution in similar electrodeposition experiments.